THE UNIVERSITY OF HULL

Quantitative Morphology of Galaxy Clusters at X-ray Wavelengths

being a Thesis submitted for the Master of Science

in the University of Hull

by

Laura Hunt, BSc

September 2021

Acknowledgements

I would like to thank my parents for their unwavering support through my academic career. My mother for giving me her determination and drive to always seek new and amazing opportunities. My father for not only inspiring my love of science but helping me to develop the patience and perseverance I need to succeed in it. My supervisor, Kevin, for his invaluable encouragement and feedback for which I would be lost without. Without these people my Masters degree would not have been possible, you all have my ceaseless gratitude and admiration and I hope you all know how much you have helped me in the path to achieving my dreams.

Declaration of Originality

This thesis is submitted in partial fulfilment of the degree of Master of Science from the University of Hull. I declare that the work undertaken in this thesis is original and my own and was carried out under the supervision of Dr Kevin Pimbblet and Dr Brad Gibson. Where work, results, or ideas have been taken from other sources, those sources are explicitly referenced.

Candidates signature:

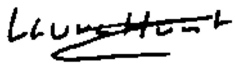

Date: 13/09/2021

Abstract

We apply quantitative morphology techniques to X-ray imaging of clusters of galaxies to determine correlation between calculated parameters (CAS, Gini and M_{20}) and features such as bow shocks, cold fronts, gas sloshing, Kelvin-Helmholtz instabilities (KHI), X-ray cavities and relaxed/disturbed clusters. In order to do this we create a novel sample of 51 cluster images from archival data such as $Chandra$ and $XMM-Newton$ based on selection criteria spanning a redshift $0.01 < z < 0.07$ and X-ray luminosity $L_x > 1 \times 10^{44}$ ergs s^{-1}. We process the original images, and remove foreground sources and CCD gaps, and apply adaptive kernel smoothing on the central 3 Mpc of the clusters which is determined using an asymmetry technique to weight the luminosity centroid of the image. For each image we calculate the concentration of light C, the asymmetry index A, the clumpiness parameter S, the Gini coefficient G and the M_{20} parameter. We attempt to correlate these results with the physical features present and demonstrate that the presence of bow shocks is correlated with higher M_{20} and lower C and S, cavities correlate with low G and S, cold fronts show low S and G and higher M_{20}, low S and high M_{20} correlate with gas sloshing and clusters that exhibit KHI have high S values.

Contents

List of Figures

List of Tables

1. Introduction

Matter in the Universe is distributed amongst clusters of galaxies and cosmic filaments which are separated by vast voids of mostly empty space (Geller & Huchra, 1989; Bond et al., 1996; Pogosyan et al., 1998; Sousbie, 2011; Cautun et al., 2014). Gravitation is the driving factor behind this distribution of matter as it is the cause of the accretion of smaller objects onto larger objects of which clusters of galaxies are the largest (Cole & Lacey, 1996). These clusters are comprised of an amalgamation of anywhere between hundreds to thousands of galaxies and the intracluster medium (ICM) with dark matter making up the vast majority of the mass in the clusters. The ICM is comprised of super-heated gas called plasma that permeates the cluster and emits strong X-ray radiation through the Bremsstrahlung process (Sarazin, 1986; Sarazin & Kempner, 2000; Buote, 2002). This emission allows us to observe gravitational disturbances and dynamical processes that are driven by cluster evolution and merging. Merging events deeply affect a cluster's properties through the dynamical disturbance of the ICM's density, temperature and metallicity distribution (Ferrari et al., 2005; Sauvageot et al., 2005; Kapferer et al., 2006; Markevitch & Vikhlinin, 2007). As a result of these events we can observe the formation of substructure visible in X-ray images. We can classify clusters by the different substructures that form by quantifying their morphology non-parametrically (Parekh et al., 2015).

Classifying clusters with similar substructure is useful as these classifications may form samples of clusters that can be used for studies of cosmology and dark matter. Over the last century many galaxy cluster classification systems have been developed based on a wide range of criteria. Historically, clusters are able to be categorised into one of six richness and seven distance classes (Abell, 1958). However, this can be simplified as all clusters fall into one of two categories of either regular or irregular (Abell, 1965), these classifications only determine whether a cluster exhibits a general spherical symmetry in its galaxy distribution with high central concentration or not. This can be further described by

the two-class system of dynamical state, as a regular clusters are less dynamically disturbed and are therefore called relaxed. Irregular clusters are more dynamically disturbed and are called non-relaxed/disturbed clusters.

There are also more refined classification systems based on a number of definitions. For example, clusters can be classified on their richness, which can be defined as the number of galaxies associated with a cluster. Abell (1958) describes five classes based on a richness criterion in which at least fifty galaxies in the cluster must not be more than 2 mag fainter than the third brightest galaxy. The Bautz-Morgan (Bautz & Morgan, 1970) classification uses the relative contrast between the brightest galaxy and the other galaxies in a cluster to classify it into one of five categories. This consists of three "main" classes and two intermediate classes to distinguish clusters with a centrally located cD galaxy (type I) to clusters containing no dominant galaxies (type III). The six-class system devised by Jones & Forman (1992) is often used when trying to determine whether clusters are dynamically disturbed as it describes the type of substructure present such as single, elliptical, offset centre, primary with small secondary, bimodal and complex. Clusters may also be divided into cool core or non-cool core classes as this can have significant effects on the clusters underlying environment. A cool core is the result a dense core that cools gas and is compressed by the forces of the surrounding, hotter gas (Hudson et al., 2010); this generates a cooling flow that is characterised by a higher luminosity (Fabian et al., 1994). The two-class approach is generally favoured in studies as this distinguishes dynamically disturbed and non-disturbed clusters.

These classification systems have been developed for optical imaging and have proven useful for the detection of substructuring. Of course, optical imaging is only one part of the electromagnetic spectrum. At X-ray wavelengths, we are afforded other views into cluster systems that reveal structures such as cavities. X-ray cavities are used as tracers for supermassive black holes, hence detecting the presence of these features in an automated manner is of utility to both cluster classification and their physical state at different energy regimes (Fort, 2017). Detection of the presence of specific types of substructure (e.g. cavities, bow shocks, sloshing gas, Kelvin-Helmholtz instabilities and cold fronts) is a clear next step in cluster classification. Merging processes can cause substructures such as gas sloshing, bow

shocks, KHI and cold fronts to form but the nature of the merger and the cluster's individual characteristics are what determine which structure forms. At present, arguably the best and most robust method of classification based on substructure is an in-depth analysis of individual clusters (Proust et al., 2003; McCleary et al., 2015; Lee et al., 2016; Yu et al., 2016). Whilst this approach generates an accurate analysis of individual clusters, it is simply not feasible to perform such studies on all clusters due to it being labour intensive.

Analysis of cluster images through algorithms that quantify their structure is a couple of decades old concept that has been successfully achieved in the field of galaxy morphology with the use of Concentration, Asymmetry and Smoothness (CAS) parameters (Conselice, 2003), the Gini coefficient, G (Abraham et al., 2003; Lotz et al., 2004) and M_{20} (Lotz et al., 2004). These parameters will be described in more detail in section 3. There are also surveys applying these methods to galaxy clusters in combination with other parameters. As an example, Parekh et al. (2015) uses CAS, G and M_{20} with ellipticity and Gini of the second-order moment, G_M as a robust method of distinguishing relaxed clusters from disturbed clusters and finds this to be a viable option for future studies. Ghirardini et al. (2022) uses C and G with central density, cuspiness, power-ratios and photon asymmetry to achieve similar ends. They investigate the evolution of these parameters with redshift and luminosity where they find the percentage of relaxed clusters decreases with increasing redshift. Works such as these tend to favour classification of relaxed/disturbed clusters rather than specific substructure. As a general overview they use the combination of parameters and their correlation with each other and physical structure to create thresholds in which to further classify more clusters. As the various parameters measure different manifestations of structure, hypothetically they should also be able to distinguish between the different types of substructure given sufficient observational resolution.

1.1 Cluster Substructure

Clusters grow through the accretion of galaxies, galaxy groups and cluster mergers, these events are what cause cluster substructure to form. There are various features that are great candidates for algorithmic detection as their physical structure is visible in X-ray images

and is therefore present in X-ray images. The detection of such features can provide good samples for further studies to use as they are tracers for various cluster processes. The relevant substructure features for this work include X-ray cavities, cold fronts, bow shocks, gas sloshing and Kelvin-Helmholtz instabilities (KHI) – all observed at X-ray wavelengths. In addition to the detection of these substructures, we will also attempt to systematically classify relaxed/disturbed clusters.

As an example of what we seek to automatically detect at X-ray wavelengths, X-ray cavities in clusters, as shown in Fig. 1.1, are a well studied, fairly common feature of clusters with approximately 20 percent of all clusters currently containing cavities (Boehringer et al., 1993; McNamara et al., 2000; Bîrzan et al., 2004). Cavities are formed in the presence of radio lobes which originate in the Active Galactic Nuclei (AGNs) of clusters in which mass is accreted onto a central massive black hole causing jets that inflate bubbles of superheated, radio emitting gas (Fort, 2017; Hlavacek-Larrondo et al., 2015). This causes the displacement of ambient, X-ray emitting gas which results in depressions of X-ray emission where the lobes are present (Boehringer et al., 1993; Fabian & Nulsen, 1977). However, there is also evidence to suggest cavities may be formed from the expulsion of cosmic rays from the AGNs as they form shocks around the boundaries of the bubbles of expanding gas (Mathews & Brighenti, 2007; Sijacki et al., 2008). This has important implications concerning the transfer of AGN energy to the surrounding gas through cosmic ray diffusion, namely the difference in cosmic rays interacting with hot gas compared with ordinary gas dynamics. Previous methods of detecting cavities in systematic searches include β-modelling and unsharp masking techniques (Shin et al., 2016) and the detection of X-ray surface brightness depressions (Bîrzan et al., 2004). Prominent cavities are detected in clusters such as: the Perseus cluster (Fabian et al., 2000), Abell 2052 (Blanton et al., 2001) and Hydra A (McNamara et al., 2000; David et al., 2001), these clusters are included in our sample. Cavities in these clusters are confirmed with calculation of the temperature and pressure of the ICM. Pressure is highest in the shock regions surrounding the cavities whilst this gas is generally cool in temperature (Mathews & Brighenti, 2007). However, values for ICM temperature and pressure is not widely available for all clusters yet as it requires spectroscopic analysis of a target cluster. This means a

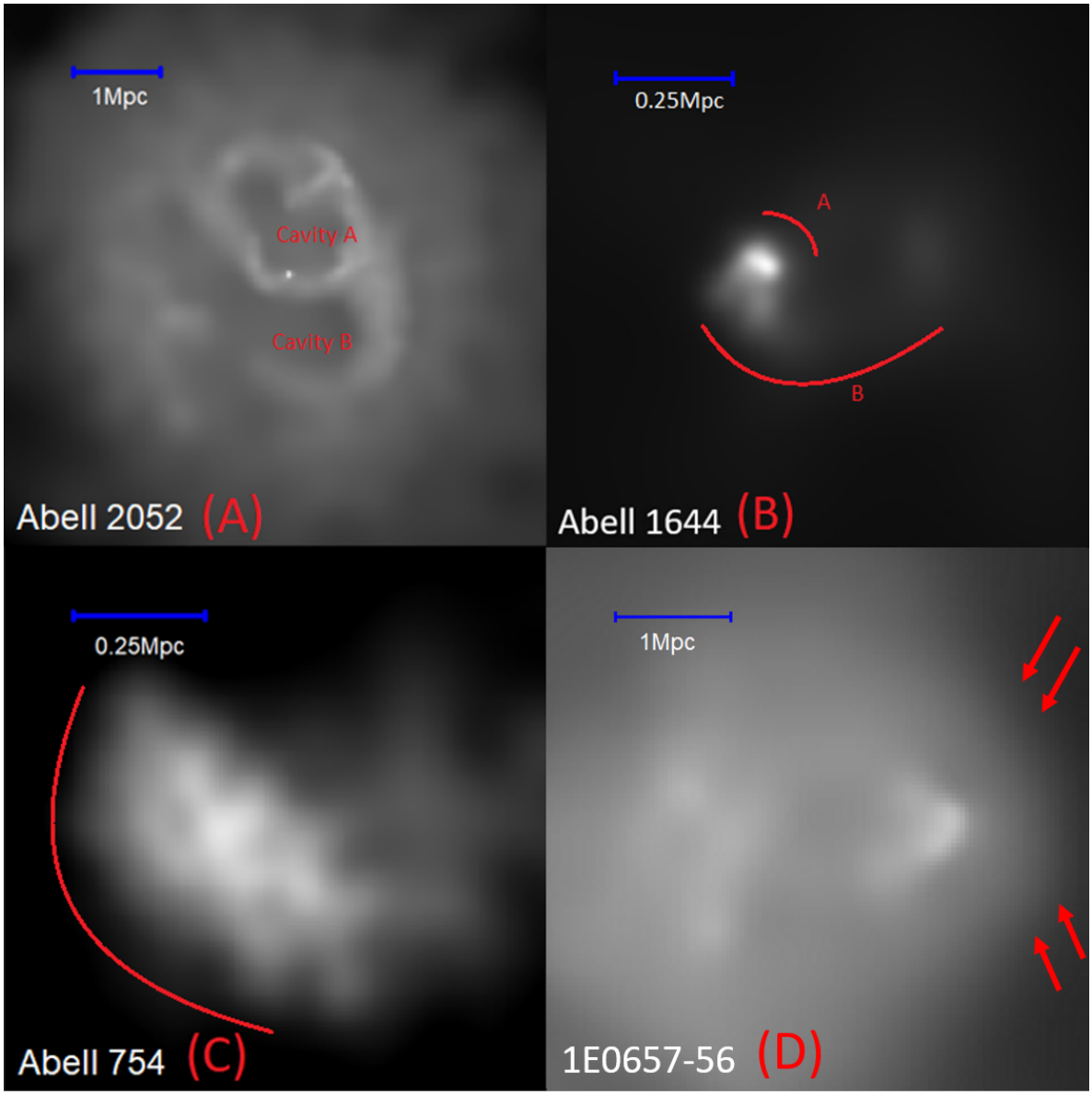

Figure 1.1: X-ray images from our sample with the addition of the cluster 1E0657-56. Produced with image processing described in section 2.2 to show how the structure appears in the final images: *(A)* shows prominent X-ray cavities labelled A and B in Abell 2052, these cavities appear dimmer than their surrounding bubbles of gas (Blanton et al., 2001); *(B)* shows the sloshing gas and cold front present in Abell 1644 (Johnson et al., 2010). Line A shows where the cold front is most prominent as there is a rapid drop off in brightness next to the main body of the cluster. The sloshing gas is visible as the main body of the cluster swings round, leaving a wake of dimmer gas behind it, shown with line B; *(C)* shows the cold fronts in Abell 754 (Markevitch et al., 2003). The cold front is shown where there is a rapid drop in pixel brightness; *(D)* shows the textbook example of a bow shock in 1E0657–56 (the Bullet Cluster) (Markevitch et al., 2002). Determining X-ray morphology is important as this visible structure can be used as a tracer when searching for clusters to be part of samples for use in other studies.

spectrum has to be produced by a telescope that is able to determine temperature such as the Chandra Advanced CCD Imaging Spectrometer (ACIS) (Giacconi et al., 2001). Generally, this requires an exposure time of a few hours which means surveys with large numbers of clusters require a lot of time and money to produce results. This is why detecting features such as cavities automatically with computational methods, like those discussed in section 3, will enable surveys of thousands of clusters that have already had X-ray images produced.

Gas sloshing in clusters as shown in Fig. 1.1 forms when a minor merging event, whether that be through the accretion of a galaxy or galaxy group onto a cluster or two clusters interacting, causes the ICM to become disturbed through gravitational processes (Roettiger et al., 1997; Markevitch et al., 2001; Ascasibar & Markevitch, 2006; Roediger et al., 2011). This appears as the gas being sloshed around the cluster core in an action comparable to knocking a wine glass. It is useful to be able to easily detect gas sloshing in clusters as the sloshing effects cluster mass measurements. This can in turn affect the calculations of the cosmological constants, as cluster properties such as total mass, shape and amount of substructure; are used to place limits on matter density Ω in the Universe (Crone et al., 1994; Richstone et al., 1992). The calculated ICM mass in clusters allows us to calculate the baryonic fraction Ω_b of the Universe. Therefore, it is imperative to detect and correct for the biases originating from sloshing to be able to accurately measure the cosmological parameters. Gas sloshing as a process can cause the formation of other features such as cold fronts.

Cold fronts, as shown in Fig. 1.1, form as a result of various processes and are characterised by a discontinuity in gas temperature. They form when cooler gas moves through hotter ambient gas which causes them to differ from shock fronts as their gas pressure remains consistently in equilibrium across the density discontinuity whereas shock fronts have a large jump in pressure across the front (Markevitch et al., 2000; Vikhlinin et al., 2001b; Markevitch & Vikhlinin, 2007). Cold fronts have been extensively studied and modelled through simulations to determine their exact origin as they are a common feature found in clusters. This is due to the processes that drive the formation of cold fronts to be fairly common, these processes include ram pressure stripping, gas sloshing and cluster mergers.

Strong density jumps in cold fronts can be found in clusters that have undergone merging (Markevitch et al., 2000, 2002; Machacek et al., 2005) however they may also present in clusters that possess a cooling flow in their centre. Cooling flows are formed where there is a region of gas that is rapidly cooling. This can cause the gas to contract and increase in density to maintain its pressure (Fabian, 1994; ZuHone et al., 2010). This higher density region can be visible in the form of a cold front where there is a temperature and density disparity (Markevitch et al., 2001; Mazzotta et al., 2001; Churazov et al., 2003; Dupke & White, 2003; Sanders et al., 2005). The detection of cold fronts provides insight into a cluster's formation history. Whether that be through a past merger like in the cases of Abell 3667 (Vikhlinin et al., 2001a,b; Owers et al., 2009) and Abell 2256 (Sun et al., 2002; Clarke et al., 2011; Breuer et al., 2020) or through gas motions in the cluster such as cooling flows and cool cores like those present in Abell 496 (Dupke & White, 2003; Roediger et al., 2012) and Abell 1795 (Markevitch et al., 2001). Cold fronts aid in determining the gas bulk velocity, potential hydrodynamic instabilities (Ichinohe et al., 2021), strength and structure of the intracluster magnetic fields, thermal conductivity, and viscosity of the ICM (Ghizzardi et al., 2010) so it is of great interest to develop an algorithm to detect them. Cold fronts caused by gas sloshing may also develop another feature known as Kelvin-Helmholtz instabilities.

Kelvin-Helmholtz instabilities (KHI), as shown in Fig. 1.1, form between two inviscid, incompressible fluids that exhibit a shear flow parallel to their boundary. Kelvin-Helmholtz rolls form as the shear velocity and density are not consistent at the interface, causing small disturbances to grow exponentially as demonstrated in Fig. 1.2 (Roediger et al., 2013a). Generally, in galaxy clusters the interface at which KHI is observed is between a galaxy and the ICM (Berlok & Pfrommer, 2019), this process is principal to the incorporation of stripped material from the galaxy into the ICM (Nulsen, 1982). Minor mergers may also trigger the formation of KHI in the presence of a sloshing cold front (Zuhone & Roediger, 2016). A number of clusters exhibit KHI as a result of sloshing such as Abell 2142 (Wang & Markevitch, 2018) and the Virgo Cluster (Roediger et al., 2013b) in which constraints are able to be placed on effective viscosity due to analysis of the KHI, a method derived by Roediger et al. (2013a). Therefore, automatic detection of KHI in clusters from image data is a powerful tool to aid

the analysis of ICM properties.

Bow shocks as shown in Fig. 1.1 are another structure formed by merging processes. They are formed when a dense, infalling gas body or subcluster moves through hot ambient gas at a speed greater than the velocity of sound (Vikhlinin et al., 2001b; Markevitch & Vikhlinin, 2007). This causes a compression of the hot gas in front of the body or subcluster and is presented as an X-ray surface brightness discontinuity. Historically, the presence of a bow shock is confirmed by observing the density, temperature, and pressure jump. Then the speed and gas pressure of the infalling body and ambient gas can be calculated. A number clusters have been verified to be containing a bow shock, such as the Bullet cluster (1E0657–56) (Markevitch et al., 2002), A3667 (Vikhlinin et al., 2001b) and A520 (Markevitch et al., 2005) to name a few. Shocks not only provide insight into the velocity and geometry of mergers (Markevitch et al., 2002) but also act as laboratories for the study of the intracluster plasma processes such as thermal conduction and electron-ion equilibration (Takizawa, 1999). In addition to this, the Bullet cluster has been used to place constraints on dark matter estimates (Markevitch et al., 2004) and is one of the most influential pieces of evidence for the existence of dark matter (Clowe et al., 2004) which will be further discussed at the end of this chapter. Therefore, it is important to be able to systematically detect bow shocks in clusters.

1.1.1 Cosmological Importance

A cluster's formation and evolution with redshift depends on the cosmological constant and the mean matter density. The higher the redshift of a cluster the more dynamically young they appear to be as merging and accretion is associated with the formation of clusters. This can be seen through the substructure present within them as merging clusters are more disturbed. Studies up to a couple of decades ago are limited to using clusters up to $z \lesssim 0.3$ as image data is limited by observational technology. However, XMM and $Chandra$ surveys provide observations of clusters out to $z \sim 1$. We choose these surveys to compare their resolutions which we discuss further, in section 4 and 5. This gives us great insight into clusters at a higher redshift, enabling us to build a broader picture of cluster evolution and formation. Establishing a wide redshift range helps to consolidate our ideas of cluster formation as higher

redshifts provide us with dynamically younger clusters and lower redshifted clusters are older and more evolved. Therefore, assembling a collage of clusters at all redshifts brings us closer to understanding the cosmology of our universe as a whole.

As described previously, clusters are vital in measuring cosmological constants as they provide self consistent laboratories that are perfect to study various cosmological properties. Previous studies have found that the ratio of gas mass to total mass in massive clusters can provide powerful insight into cosmology (White et al., 1993; Allen et al., 2004). This gas mass fraction, f_{gas}, should approximately match the cosmic baryon fraction, Ω_b/Ω_m (Borgani & Kravtsov, 2011) in very massive clusters where the mass of hot, X-ray emitting gas greatly exceeds the mass of colder gas and star mass (Lin & Mohr, 2004). Recently there have been reliable predictions of the baryonic depletion of clusters which when combined with measurements of f_{gas} and constraints on Ω_b provide a great method of constraint for the cosmic matter density, Ω_m.

Not only are clusters useful in the measurement of the cosmological constants but they can be used as powerful tools in the study of dark matter. Historically, clusters appear to have deeper potential wells than their inferred baryonic mass could account for, this has provided argument for the existence of dark matter halos around the clusters to make up for this discrepancy (Zwicky, 1933; Peebles, 1982; Blumenthal et al., 1984; Davis et al., 1985). Studying the cluster 1E0657–56 has enabled a weak lensing mass reconstruction because of the ram pressure stripping away the X-ray gas from the present galaxies. This stripping, triggered by the collision of a sub-cluster into the main body of the cluster, has formed a textbook example of a bow shock (Markevitch et al., 2002). As highlighted by Clowe et al. (2006), methods of dark matter detection have previously used objects that required the assumption of symmetry, hydrostatic equilibrium and/or the centre of mass location to be known. This brought about counterarguments which Clowe et al. (2004) determined could only be resolved with a system in which baryonic matter was separated from the inferred dark matter. Thus, the Bullet cluster is an ideal candidate as Clowe et al. (2004) observes offsets between the lensing mass peaks and the peaks of the dominant visible mass. Therefore, directly demonstrating the presence of a dominant dark matter component. Automatic classification of substructure

could directly aid surveys that use these structures to calculate cosmological constants.

1.1.2 Methods of Quantification

There are various methods of quantifying cluster morphology however many methods require laborious techniques that only make quantification possible for small surveys or individual cluster studies. Some methods include the caustic technique which aims to estimate the escape velocity of cluster galaxies from the cluster centre to a few times the virial radius and can be used to estimate mass and gravitational potential profiles of clusters to radii that extend the cluster infall region (Yu et al., 2015). Weak gravitational lensing can be used to calculate the mass along a line of sight in a cluster (Clowe et al., 2004). Both of these methods determine the mass profile of a cluster beyond the virial radius, however when compared with each other their estimations are only 30% similar (Geller et al., 2013). The power ratio method aims to quantitatively classify clusters of different, "dynamically relevant" morphology in direct relation to their dynamical state as indicated by their gravitational potential and ultimately produce a simple, quantitative scheme of categorisation (Buote & Tsai, 1995). They distinguish clusters based on their morphologies by calculating the multi-pole moments of the X-ray surface brightness in which they find correlation with higher redshift and the power ratios P_3/P_0 and P_4/P_0. While useful tools, these techniques are far too time-consuming to calculate for large samples of clusters. Algorithms that classify clusters based on their image data are able to automatically classify much larger samples.

Historically, the parameters we use in our study were first developed for the classification of galaxies. The calculation of which will be discussed further in section 3. CAS (Conselice, 2003; Lotz et al., 2004), G (Abraham et al., 2003; Lotz et al., 2004) and M_{20} (Lotz et al., 2004) parameters are able to distinguish between different morphologies of galaxies based on their image data. A comprehensive review of the history and performance of these parameters is written by Conselice (2014) which is preceded by a number of notable studies that successfully apply this technique to the classification of large samples of galaxies (Scarlata et al., 2007; Zamojski et al., 2007; Holwerda et al., 2011; Hoyos et al., 2012; Rasia et al., 2013). The application of these parameters to galaxy clusters has mostly been limited to the classification

of relaxed/disturbed clusters (Parekh et al., 2015; Ghirardini et al., 2022) or cool-core/non-cool core clusters (Ghirardini et al., 2022) and cluster mass estimation (Green et al., 2019). However, there is a noticeable lack of studies attempting to correlate specific X-ray features with these parameters.

In this work, we aim to classify X-ray images of clusters of galaxies in an automated manner to be able to detect the features noted above via correlating them with C, A, S, Gini, and M_{20}. The rest of this paper is organised as follows. Section 2.1 gives a brief introduction to the sample of clusters used in this paper. Section 2.2 gives the X-ray data reduction and image processing with point source removal and smoothing. Section 3 describes the parameters used to quantify structure. Section 4 presents the results of the parameters which will be discussed in section 5. We use H_0=70 km s^{-1} Mpc^{-1} Ω_M=0.3 and Ω_Λ=0.7, in concordance with ΛCDM, is assumed throughout.

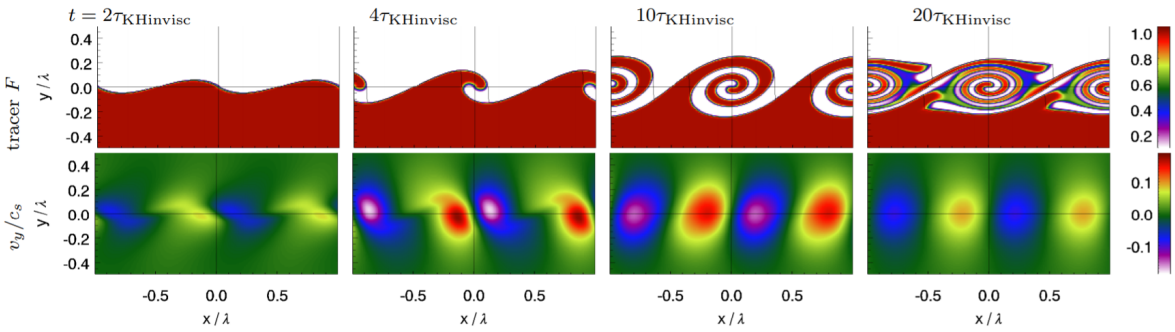

Figure 1.2: The evolution of KHI rolls shown as a fiducial KHI test through simulation by Roediger et al. (2013a). The top row shows the development of rolls at increasing time-steps and the bottom row colour-codes the vertical velocity to demonstrate the vortices produced by the Kelvin-Helmholtz rolls.

2. Cluster Images

2.1 Cluster Sample

For this work, we seek a large sample of X-ray imaged clusters of galaxies in order to apply morphological measures to and correlate with the presence of various features and substructures. We use preprocessed images from the *Chandra* and *XMM − Newton* archive and have applied image processing where necessary to clean them up, this process is described in more detail in Section 2.2. We do this because the automatic quantification process would ultimately be performed on clusters that already have compiled observations. Each cluster is detailed in Table B.1 with its corresponding Observational ID (ObsID), details of exposure and results. Additionally, the details of the observations are more thoroughly described in the referenced papers in Table 2.1. In order to place the clusters on a fair and equal footing with each other, we impose both a redshift and X-ray luminosity limit, detailed below, to yield an X-ray selected sample.

In Fig. 2.1, we show the redshift and X-ray luminosity of the sample used in this work, generated from the X-ray Clusters Database (BAX) (Sadat et al., 2004) where we searched for a sample observed previously with the *XMM − Newton* or *Chandra* telescopes, with limits set to a redshift range of $0.01 < z < 0.07$ which is chosen to eliminate low redshift contamination from potentially Galactic sources, and at the upper end cut off our sampling to keep the cluster structure standardized. An X-ray luminosity lower limit of $1{\times}10^{44}$ ergs/s is chosen so that we capture a range of luminosities, but maintain objects brighter than this limit to ensure we are able to perform reasonable morphological measures.

This yields a total of 84 clusters to work with, and across a range of *Chandra* and *XMM − Newton* images. However, 33 of these clusters do not have high enough quality images available so the total number of clusters in the sample is reduced to 51. This is determined by visual inspection and checking the observation logs available with the images in the *Chandra* and *XMM − Newton* archive. As the high spatial resolution of images

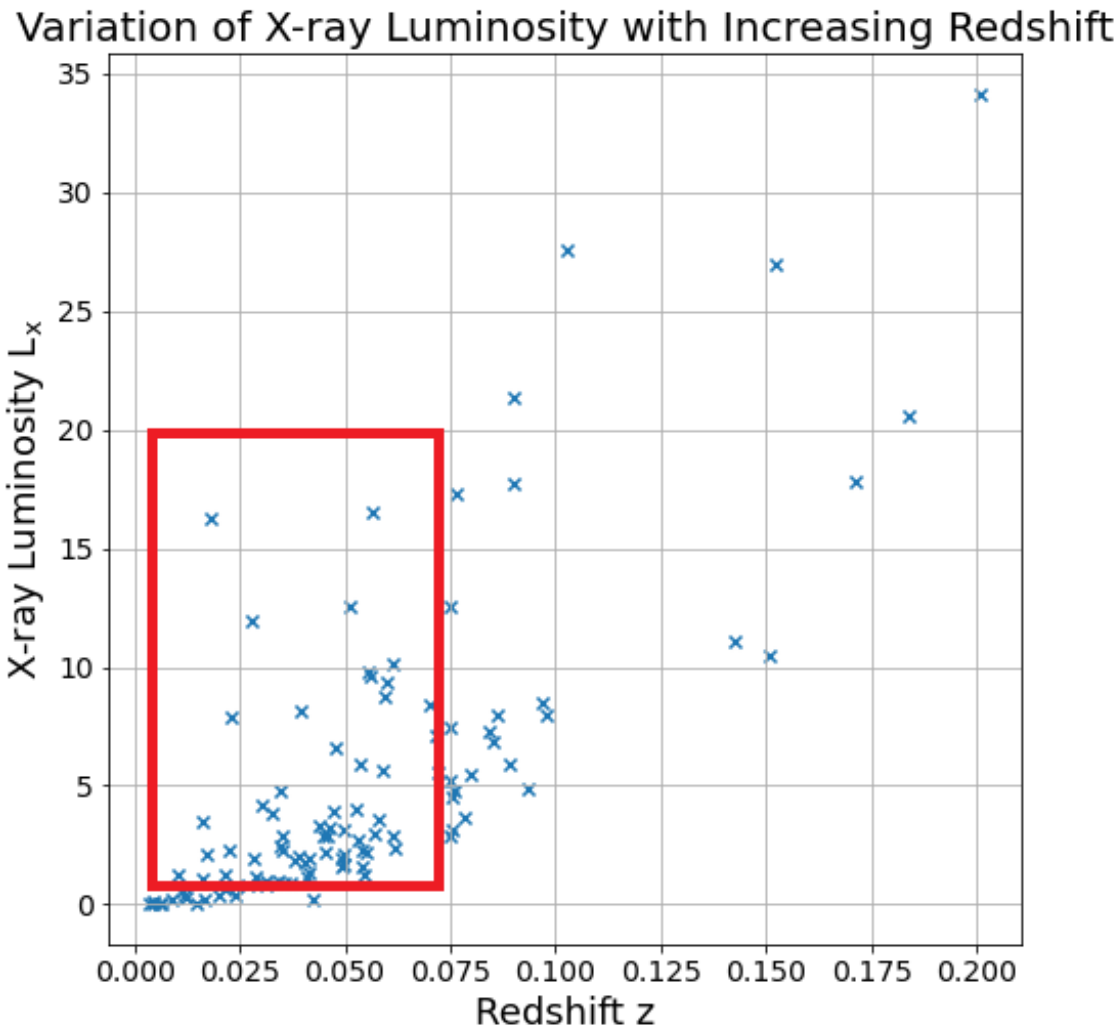

Figure 2.1: Redshift - X-ray luminosity diagram for BAX showing our final cluster sample. The sample is contained within limits shown in red which are chosen to provide the widest range of redshift without including contamination from Galactic sources at lower redshifts $z < 0.01$, and poorer quality observations at higher redshifts $z > 0.07$. We choose a lower limit of $1{\times}10^{44}$ ergs/s to ensure clusters are bright enough for structure analysis.

plays a significant part in the visibility of substructure within the clusters, *Chandra* and $XMM-Newton$ images are used for our study. In total, 14 clusters are imaged by *Chandra* (resolution of 0.492" per pixel) and 37 are from the $XMM-Newton$ (resolution of 1.1" per pixel). Though these are not necessarily limiting factors of resolution. Table 2.1 shows classifications of whether structure is present or not. Where there is the presence of a citation, this means the cluster's structure has been confirmed by the study referenced. Where there is no citation, the clusters have been classified by visual inspection. This is not ideal, however more accurate classification of all 51 clusters through methods such as modelling are beyond the scope of this work. The visual inspection consists of checking the cluster images by-eye for obvious signs of structure, this means more subtle structure may missed. This is further discussed in Section 5.

Cluster	z	Relaxed	Bow Shock	Cavity	Cold Front	Sloshing	KHI
A1644	0.047	✗[1]	✓	✓	✓[2]	✓[2]	✗
A1668	0.063		✗	✓[3]	✗	✗	✗
A1795	0.062	✓[1]	✗	✓[4]	✓[5]	✓[6]	✗
A1991	0.059	✓[7]	✓	✓[4]	✓	✗	✗
A2052	0.035	✓[1]	✗	✓[4]	✓	✓	✓
A2124	0.066	✓[8]	✓	✗	✓	✗	✗
A2589	0.041	✓[1]	✗	✓[4]	✓	✗	✗
A2626	0.055	✓[9]	✗	✓[4]	✓	✓	✓
A3266	0.059		✗[1]	✗	✓[10]	✗	✗
A4059	0.048	✓[1]	✗	✓[4]	✓	✓	✗
AWM7	0.017		✗	✓	✓[4]	✓	✗
CYGNUSA	0.056		✗	✓	✗[4]	✗	✗
OPHIUCHU	0.028		✗	✓[4]	✓[10]	✓[11]	✗
SC1329-313	0.048		✗	✗	✗	✗	✗
A0119	0.044	✗[1]	✗	✗	✓	✓	✗
A0262	0.016	✓[12]	✗	✓[4]	✓[10]	✗	✓
A0426	0.018	✓[17]	✗	✓[4]	✓[13]	✓[18]	✓[18]
A0576	0.039	✗[1]	✗	✗[15]	✓[10]	✗	✗
A0602	0.062		✗	✗	✗	✗	✗

[1] Parekh et al. (2015)
[2] Johnson et al. (2010)
[3] Pasini et al. (2021)
[4] Shin et al. (2016)
[5] Markevitch et al. (2001)
[6] Fabian et al. (2001)
[7] Wen & Han (2013)
[8] Marini et al. (2004)
[9] Laganá et al. (2019)
[10] Ghizzardi et al. (2010)
[11] Werner et al. (2016)
[12] Hradecky et al. (2000)
[13] Ichinohe et al. (2019)

Table 2.1 continued from previous page

Cluster	z	Relaxed	Bow Shock	Cavity	Cold Front	Sloshing	KHI
A0754	0.054	✗[1]	✓[14]	✗	✓[10]	✗	✓
A0780	0.054	✓[1]	✗	✓[4]	✗	✗	✓
A1069	0.065		✗	✗	✗	✗	✗
A1656	0.023	✗[15]	✓[20]	✗	✓[20]	✓[20]	✗
A1736	0.046	✓[1]	✗	✓	✓	✓	✗
A1831	0.062		✗	✓	✗	✗	✗
A1837	0.070		✗	✓	✓	✗	✗
A2063	0.035	✓[1]	✗	✗[20]	✗[10]	✗	✓
A2147	0.035	✗[1]	✗	✗	✓	✗	✗
A2199	0.030	✗[1]	✗	✓[4]	✓[10]	✓[16]	✓
A2256	0.058	✗[1]	✓	✓	✓[10]	✓	✗
A2319	0.056	✗[1]	✓	✓	✓[10]	✓[17]	✓[22]
A2622	0.062		✗	✓	✗	✗	✗
A2634	0.031		✗	✗	✗	✗	✗
A2657	0.040		✗	✓	✓	✓	✗
A3122	0.064		✗	✓	✓	✓	✗
A3391	0.051	✗[1]	✗	✓	✓	✗	✓
A3490	0.069		✗	✗	✗	✗	✗
A3497	0.068		✗	✗	✓	✓	✗
A3526	0.011		✗	✓[4]	✓[10]	✓	✓
A3530	0.054		✗	✗	✗	✗	✗
A3532	0.055	✓[9]	✗	✓	✗[10]	✗	✗
A3558	0.048	✗[1]	✗	✗	✓[10]	✗	✓
A3562	0.049	✗[1]	✓	✓	✗[10]	✗	✓

[14] Markevitch et al. (2003)
[15] Churazov et al. (2021)
[16] Nulsen et al. (2013)
[17] Ichinohe et al. (2021)

Table 2.1 continued from previous page

Cluster	z	Relaxed	Bow Shock	Cavity	Cold Front	Sloshing	KHI
A3571	0.039	✓[1]	✗	✗[15]	✗[10]	✗	✓
A3651	0.060		✗	✗	✗	✗	✗
A3667	0.056	✗[1]	✓[18]	✓	✓	✗	✓
A3716	0.046		✗	✓	✓	✓	✗
ESO235	0.049		✗	✗	✗	✗	✗
RXCJ0102	0.057	✓[1]	✗	✓	✗	✓[19]	✓[20]
RXCJ0413	0.050		✗	✓	✓	✓	✗
RXCJ2205	0.058		✗	✗	✗	✗	✗
RXCJ2347	0.030	✗[1]	✗	✗[20]	✗[10]	✗	✓
Total		15	9	31	32	21	17

Table 2.1: The cluster sample, split into two sections: the first are all observed by *Chandra* and the second is *XMM − Newton*. (1) Clusters name; (2) redshift z; (3) dynamical state of cluster (relaxed or disturbed) based on literature; (4)-(8) evidence of substructure based on literature evidence or by eye. Clusters without literature evidence of substructure have no labelled reference.

[18] Vikhlinin et al. (2001a)

[19] Randall et al. (2010)

[20] Fujita et al. (2002)

2.2 Data Processing

Images are from $Chandra$ and $XMM-Newton$ archives that provide pre-processed images compiled from the raw events files. Each observation is completed for a specific paper requested by an observer that has detailed the quality of the observation. We choose these images rather fully processing our own as ultimately, the purpose of our work is to detail an automatic method of morphology quantification that will be able to use large surveys of images like these that have already been produced but require a method of quantifying their structure for further study. Table. B.1 details observational IDs (ObsID) and exposure times for each cluster. Some of the data (especially XMM) still have chip gaps that need to be dealt with in a systematic manner before we are able to apply morphological measurements. Since foreground point sources in these images might strongly influence the resultant morphological measurements, we similarly need to remove these before making any measurements. As the clusters have different exposure times, the brightness varies between images and the images must be standardised.

Image processing is completed in the following steps:

1. The images are filtered first by energy band to limit the sample to 0.5keV-3keV as this optimizes the signal-to-noise ratio from the given cluster, this is done with simple `Python` script that is able to iterate over all of the images, and uses their `.fits` file information to calculate the respective energies;

2. The images are then filtered again with the Grubbs's test (Grubbs, 1950) to identify and cap any outlying pixels. These outliers are found and set to the next maximum pixel value;

3. Images are initially cropped to a scale of ~3Mpc to remove as much of the background as possible and to enable centroiding prior to final cropping step 6;

4. Point sources and CCD gaps are identified and removed with the `fixpix` task in `IRAF`;

5. Images are smoothed with the standard Adaptive Kernel Smoothing (AKS) algorithm `asmooth`;

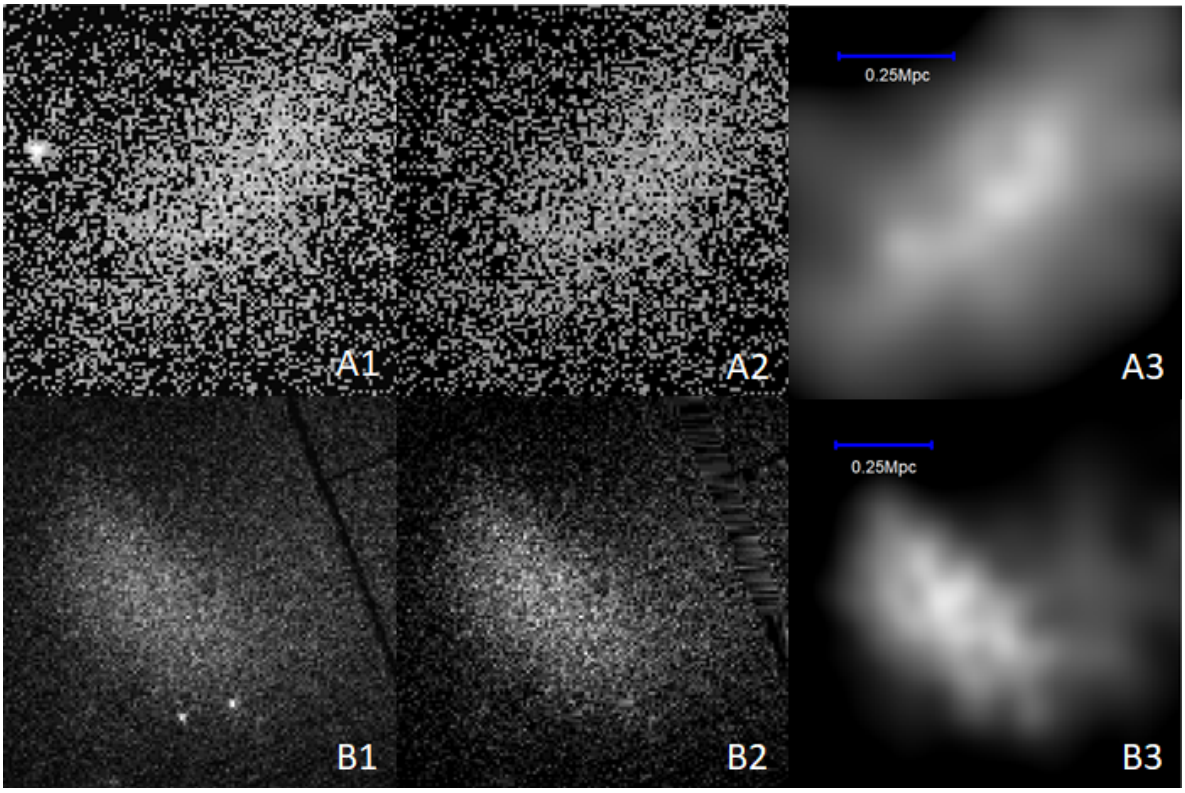

Figure 2.2: Images from left to right show the data processing approach applied to two clusters (A0602 – labelled A, and A0745 – labelled B) and what the final outcome is. A1 and B1 show the original images and A3 and B3 show the final smoothed images. A1 and B1 have point sources that are removed by interpolating across the affected pixels. A2 and B2 show that the point sources have been removed. B1 and B2 show how the 'dead' pixels in the CCD gap are interpolated across.

6. Images are re-centered using the Asymmetry Index (Conselice et al., 2003) and cropped to a scale of ~100kpc to place all clusters onto a common fixed metric scale. Note that this step is distinct from step 3 since the above step is purely undertaken to provide a limit to which the centroiding is determined (i.e., this step).

(Note that all of these steps are completed a second time without the penultimate smoothing step to produce a second sample of unsmoothed images for calculating the Clumpiness parameter as this requires smoothing by a Gaussian Kernel).

Point sources are identified by finding groups of pixels higher than 3σ over the local median. The local median is determined by dividing the image into a 9x9 segment grid and calculating the median for each segment. The affected pixels have their coordinates written to a file. These files are then run through the `fixpix` task in `IRAF` which interpolates across

the areas of badpixels to remove any image artefacts in the smoothed images. This process can be seen in Fig. 2.2. These point sources are removed as they can affect the results of our parameters. For example, a point source could increase the Smoothness value as the cluster would appear to be clumpier than it actually is due to the point source's localized light. CCD gaps are detected by finding the "dead" pixels of each image's corresponding exposure map and also written to a file. Some clusters still have visible CCD gaps after this process, these are removed from our original sample of 84. Unfortunately, our process of removing point sources was unable to remove all of them and in light of a severely reduced sample size, we chose to include them in our results. This is discussed further in section 5.

Smoothing is performed on the X-ray images by using the Adaptive Kernel Smoothing algorithm, `asmooth` (Ebeling et al., 2006). `asmooth` uses a "uniform significance approach" which determines the local size of the kernel from the requirement that, at each position within the image, the signal-to-noise ratio of the counts under the kernel and above the background, must reach (but not greatly exceed) a certain preset minimum, τ_{min}. Images with dimensions less than (100x100) pixels used a $\tau_{min} = 2$, images with dimensions greater than (100x100) but less than (200x200) pixels used a $\tau_{min} = 3$ and images with dimensions greater than (200x200) pixels used a $\tau_{min} = 4$. This is because the images with larger dimensions have a larger resolution and therefore the relevant structure covers a larger area of pixels. To combat this a larger τ_{min} is chosen so the kernel requires more pixels to be under it to reach a larger signal-to-noise ratio, this prevents under-smoothing. The result of this can be seen in Fig. 2.2.

Once smoothed, the images are run through an algorithm that calculates the Asymmetry Index (shown in Eq. 3.2; see also (Conselice et al., 2003) of various points around the cluster's centroid in a jittering motion. The point with the lowest Asymmetry value is taken as the new centre and a final crop is performed as per step 6, above.

3. Analysis

The parameters used in this paper are most commonly used in the study of galaxy morphology (Conselice, 2003; Lotz et al., 2004; Abraham et al., 2003). They can also be used in combination with each other to classify galaxies (Conselice, 2014) and clusters (Parekh et al., 2015), and here we apply them to the final X-ray imaging in order to be able to correlate them with the presence of features noted in the literature about these clusters (cf., Table 2.1). Below, we briefly detail each morphological measurement made on our sample.

3.1 Light Concentration

The light concentration C parameter measures how the pixel flux is distributed from the centre of the cluster. It finds the ratio between the radii at which 20% and 80% of the clusters light is contained (Conselice, 2003).

$$C = 5 \log \frac{r_{80}}{r_{20}} \tag{3.1}$$

Where r_{80} is the radius that contains 80% of the cluster's light and r_{20} is the radius that contains 20% of the light. The larger the C value, the more light is contained in the smaller of the two radii. In other words, the higher the C value the more concentrated the light is in the centre of the cluster. Typical values for C range between 2.0-5.0 for clusters, non-relaxed clusters show lower values of C as their light tends not to be concentrated in the centre (Parekh et al., 2015).

3.2 Asymmetry Index

The Asymmetry Index A measures how asymmetric a cluster is. It is calculated by rotating the image of a cluster by 180 deg around the cluster centre (x_c, y_c), subtracting the individual pixel values of the rotated image from the original image and finding the sum of this subtracted image (Conselice, 2003).

$$A = \frac{\sum |I_{(x,y)} - R_{(x,y)}|}{\sum |I_{(x,y)}|} \tag{3.2}$$

Where I is the original image R is the rotated image. The images must be background corrected before A is calculated, this has been achieved with the Python package `Photutils` background estimator. Higher A values show that the cluster is more asymmetric. Typical values for clusters range between 0.0-0.8 (Parekh et al., 2015).

3.3 Smoothness

The Smoothness S parameter (also known as clumpiness) describes the fraction of light in a cluster that is contained in clumpy distributions. It is calculated in this paper by smoothing an image of a cluster with a Gaussian kernel σ to produce a smoothed image which is then subtracted from the original to leave a residual map of the high frequency structures. S is then found summing this residual image and dividing by the sum of the original (Conselice, 2003).

$$S = \frac{\sum |I_{(x,y)} - B_{(x,y)}|}{\sum |I_{(x,y)}|} \tag{3.3}$$

Where $I_{(x,y)}$ is a pixel in the original image and $B_{(x,y)}$ is a pixel in the smoothed image. The standard deviation of the Gaussian smoothing kernel is set to $\sigma = 3$. Similarly to A, the images must be background corrected before S is calculated, which again has been achieved with the Python package `Photutils` background estimator. The larger S is, the more clumpy the structure is. We discuss the ability of Smoothness to predict not only clumps, but features such as cold fronts, sloshing and X-ray cavities specifically in section 5.

3.4 The Gini Coefficient

The Gini coefficient G is used to calculate the distribution of pixel flux (Abraham et al., 2003; Lotz et al., 2004). When used in the study of galaxy morphology G is described as the ratio of the area between the Lorenz curve and the curve of uniform equality, as shown in Fig. 3.1. The Lorenz curve (Lorenz, 1905) is defined as:

$$L(p) = \frac{1}{\bar{X}} \int_0^p F^{-1}(u) du \tag{3.4}$$

where $\bar{X}$ is the mean of over all of the pixel flux, p is the percentage of lowest value pixel and $F(x)$ is the cumulative distribution function. The Gini coefficient is then defined as the

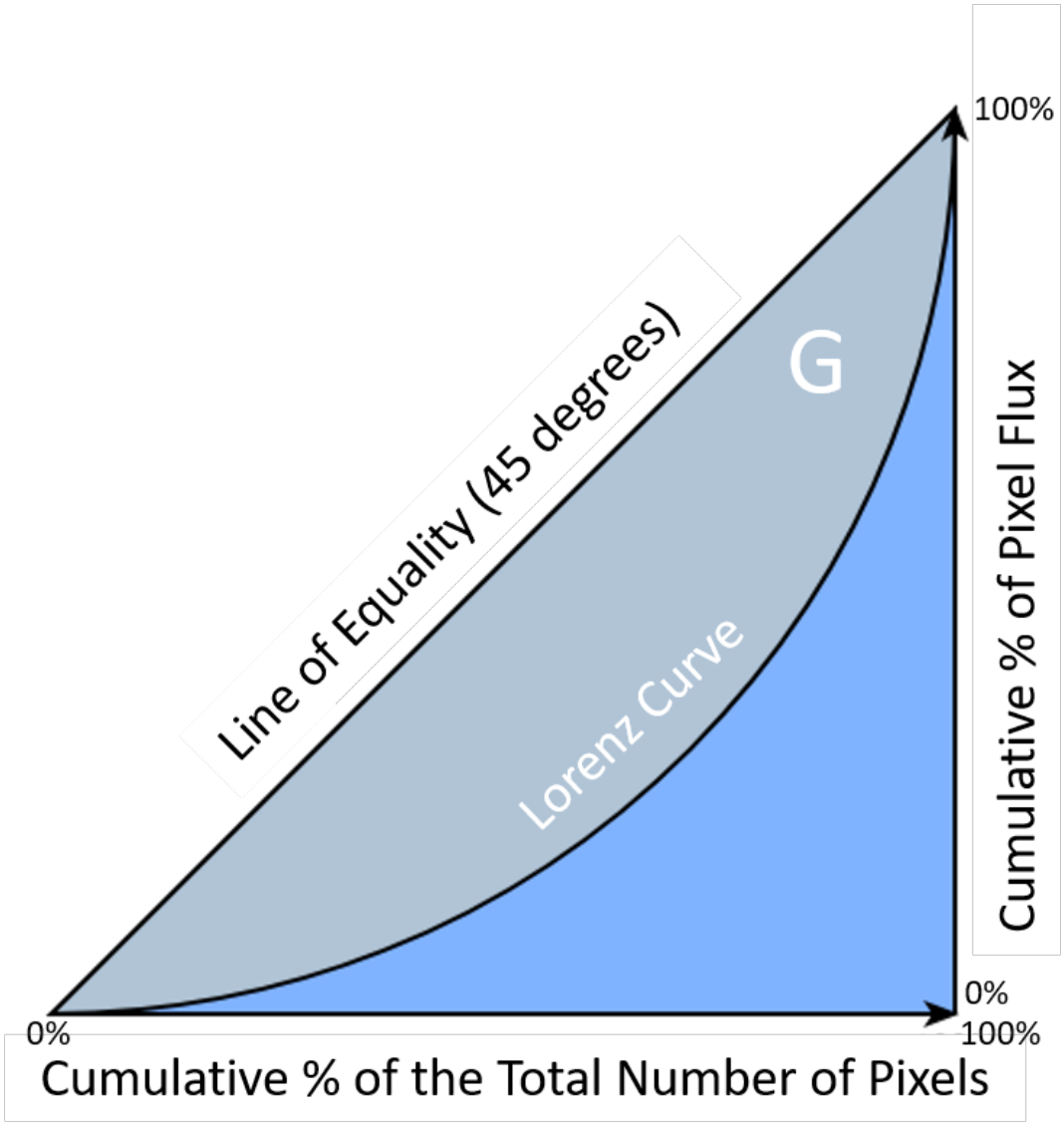

Figure 3.1: A Lorenz curve (Lorenz, 1905) represents the ratio between the total wealth and total population of a sample. In the case of a cluster or galaxy image it represents how the pixel flux is distributed across the image. The Gini coefficient is equal to the area between the Lorenz curve and the line of equality, shown as G on the graph. The line of equality is where the pixel flux is totally evenly distributed amongst all the pixels so they are all the same value.

mean of the absolute difference between all pixels X_i:

$$G = \frac{1}{\bar{X}n(n-1)} \sum_{i}^{n} (2i - n - 1)X_i \tag{3.5}$$

where n is the number of pixels in the galaxy image and i is the index for each pixel. The lower the G, the more evenly the pixel flux is distributed across the cluster as the area between the Lorenz curve and the line of equality is smaller. For example, if the pixel flux is more evenly distributed like in a diffuse elliptical galaxy, the G value will be lower than that of a spiral galaxy as there is a large disparity across the pixels between the arms and the background. The Gini coefficient differs from Concentration because the flux does not need to be in the centre, rather it quantifies how the flux varies across the entire cluster. This means it has a similar goal to Smoothness as they both quantify spatial variation in flux however in past studies Gini has been deemed to be more accurate at predicting morphology in clusters as Smoothness is more sensitive to bad signal-to-noise ratios (Parekh et al., 2015).

3.5 Second-Order Moment of Light

The second-order moment of light M_{20} finds the distribution of light in a similar way to C but M_{20} does not rely on the light being concentrated in the centre of the cluster. M_{20} is calculated by finding the total second-order moment M_{tot}, which is defined as the flux in each pixel f_i multiplied by the squared distance to the centre of the cluster, all summed over the total pixels in the cluster (Lotz et al., 2004).

$$M_{tot} = \sum_{i}^{n} M_i = \sum_{i}^{n} f_i \cdot \left((x_i - x_c)^2 + (y_i - y_c)^2 \right) \tag{3.6}$$

Where x_c, y_c is the cluster centre, which is determined by finding the point where A is minimised.

M_{20} is then calculated as the second-order moment of the brightest 20% of the flux in the cluster. The clusters pixels are rank-ordered by flux, summed M_i over the brightest pixels until the sum of brightest pixels is equal to 20% of the total flux. Finally, normalising by M_{tot} to find M_{20}.

$$M_{20} \equiv \log 10 \left(\frac{\sum_i M_i}{M_{tot}} \right) \text{while} \sum_i f_i < 0.2 f_{tot} \tag{3.7}$$

Where f_{tot} is the total flux of the cluster and f_i represents the fluxes of each rank-ordered pixel i. The higher the M_{20} value, the more evenly the flux is distributed over the pixels.

4. Results

Here, we present our main results that correlate the measurements made in the previous section with the features (e.g., bow shocks, etc.) noted from Table 2.1. Our results are broken down into correlations between parameters for the different types of substructure and evaluated with a standard two-sample Kolmogorov-Smirnov (K-S) test (Fasano & Franceschini, 1987). The full list of calculated parameters for each cluster can be found in Table B.1, the medians and standard errors for each classification can be found in Table B.2 and the outcomes of these K-S tests are presented in Table 4.1.

The K-S test can be used to calculate the difference between two samples. The null hypothesis of the K-S test predicts that the two samples are identical. For our data this would mean the results of our parameters indicate that it is not possible to predict whether a cluster has a particular feature or not as the samples are too similar. This can be described as statistical similarity. Therefore, the two-sample K-S test aims to prove how significantly different two samples are. It does this by calculating the K-S statistic and the p-value for each two samples. Essentially, these values describe how much of one sample is statistically different from the other sample. The p-value is the probability that the two samples are the same, any value lower than 0.1 means the samples are statistically different as the null hypothesis can be ignored. It is determined by the K-S statistic which quantifies the distance between the empirical distribution functions of the two samples, the smaller the value the more similar the samples are. The outcomes of these K-S tests are presented in Table 4.1.

In the enumerated list below, we summarize our findings. Our results are presented visually for all clusters in Fig. 4.1-4.6. Our results are also separated into *Chandra* and $XMM-Newton$ samples in Fig. C.1-C.6 and Fig. C.7-C.12 respectively with well-known clusters marked. We do this to compare the different resolutions of the telescopes. We discuss these findings in section 5.

1. Some general correlations between clusters include:

(a) The strongest correlations for clusters independent of structure is between C, G and M_{20}. Clusters with high M_{20} always tend towards a lower C and G. This is because clusters with high M_{20} have a more even light distribution, this correlates to low C and G values as the light is evenly distributed. These trends have been noted in past studies (Parekh et al., 2015; Conselice, 2014).

(b) Clusters tend to be more symmetric however clusters with higher M_{20} seem to be more asymmetric as they have higher A values.

(c) Similarly, clusters with low concentration seem to display higher asymmetry.

2. Clusters with bow shocks present show high disparities in pixel flux distribution where the X-ray emitting gas is compressed along the border of the front. This is reflected in the M_{20}, S and C parameters shown in Fig. 4.1. Clusters in the sample with bow shocks present have higher M_{20} values showing a concentration of light that is not necessarily associated with the cluster centre like with C. As C and G are lower in the clusters with bow shocks, this seems to indicate the clusters have an even light distribution.

3. Clusters with X-ray cavities show a tendency to have higher G and M_{20} values, shown in Fig. 4.2. This reflects the uneven light distribution caused by the voids from where X-ray emitting gas has been displaced by the cavities. However, the S value shows clusters with and without cavities are indistinguishable which is an unexpected outcome. The K-S test for M_{20} shows that the sample is statistically different as the p-value is 0.089 which is lower than the 0.1 threshold.

4. Cold fronts, similarly to bow shocks, have high disparities in pixel flux distribution along the front's edge. M_{20} is higher whereas C and G are lower in clusters with cold fronts, shown in Fig. 4.3. This shows there is a relatively even distribution of light throughout the cluster. These results show similarity for the clusters with bow shocks which is to be expected as bow shocks usually have cold fronts. The p-value for C is 0.039 which shows the samples have a statistical difference.

5. Gas sloshing is presented in Fig. 4.4. The difference in samples is not as prominent as other structure though there is a slightly lower G and higher C for sloshing clusters.

This lower value for G corresponds with the lower G in cold fronts as clusters with sloshing usually exhibit a cold front. The higher C value could be due to the centre of the cluster being brighter than the surrounding sloshing gas.

6. Clusters with Kelvin-Helmholtz instabilities show low S values with a very significant difference between the samples. The M_{20} values are lower in clusters with KHI present, this correlates with high G and C values, shown in Fig. 4.5. Low S values are an unexpected result as the KHI should appear as clumpy, however the low M_{20} and G values show high levels of disparity of light between the pixels, this shows an uneven light distribution. K-S values support this for G, C and M_{20} as their respective p-values are 0.055 0.006 and 0.049, showing the clusters with and without KHI are significantly different.

7. Fig. 4.6 only shows clusters that have been confirmed with past literature to be relaxed or disturbed, as the nature of a cluster's disturbance is not necessarily visible by eye. Therefore, clusters without a confirmation of classification have been left off the figure. The samples of the relaxed and disturbed clusters show difference with relaxed clusters having lower M_{20} values and much higher G values.

	C	A	S	G	M_{20}
Structure	Stat, P-Val	Stat, P-Val	Stat, P-Val	Stat, P-Val	Stat, P-Val
Bow Shocks	0.290, 0.412	0.195, 0.849	0.280, 0.470	0.407, 0.105	0.383, 0.146
Cavities	0.169, 0.807	0.263, 0.304	0.173, 0.786	0.234, 0.444	0.342, 0.089
Cold Fronts	0.377, 0.039	0.189, 0.669	0.140, 0.926	0.283, 0.213	0.303, 0.156
Gas Sloshing	0.229, 0.464	0.205, 0.600	0.29, 0.202	0.152, 0.892	0.171, 0.794
KHI	0.394, 0.055	0.222, 0.594	0.367, 0.089	0.500, 0.006	0.400, 0.049
Relaxed	0.231, 0.782	0.214, 0.814	0.247, 0.712	0.264, 0.620	0.401, 0.182

Table 4.1: K-S probability for the different samples of substructure. Each of the 5 parameters (CAS, G and M_{20} have their respective K-S statistic and p-value displayed. Categorically, these results show that the every classification of structure is indistinguishable. Results that show a statistical difference are C, G and M_{20} for KHI clusters as their p-values are 0.055, 0.089 and 0.049 respectively. Cold fronts have a p-value for C of 0.039 and cavities have a p-value for M_{20} of 0.089, this shows statistical difference between the clusters that have these structures and those that do not. As stated previously, p-values lower than 0.1 mean two samples show statistical difference.

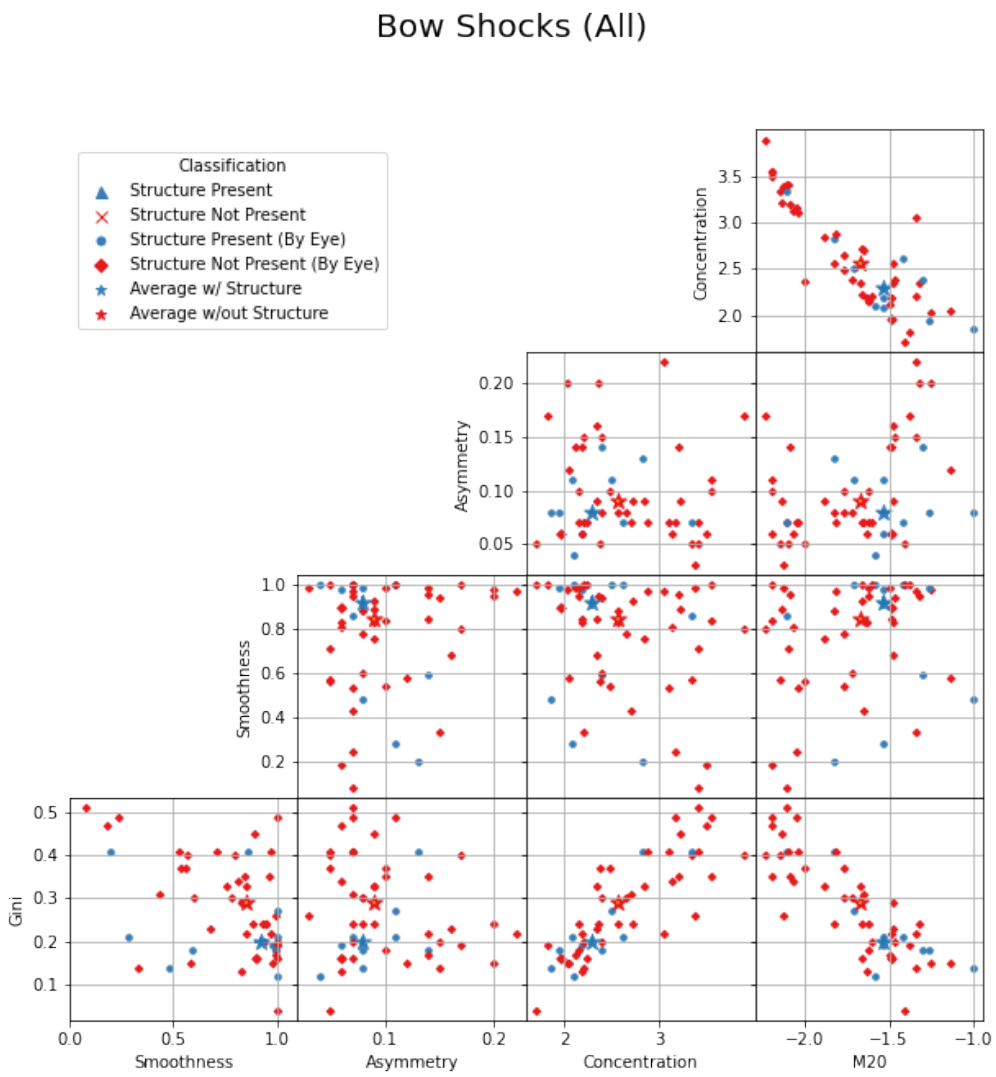

Figure 4.1: Clusters with bow shocks show higher values in the M_{20} and lower values for G and C parameters.

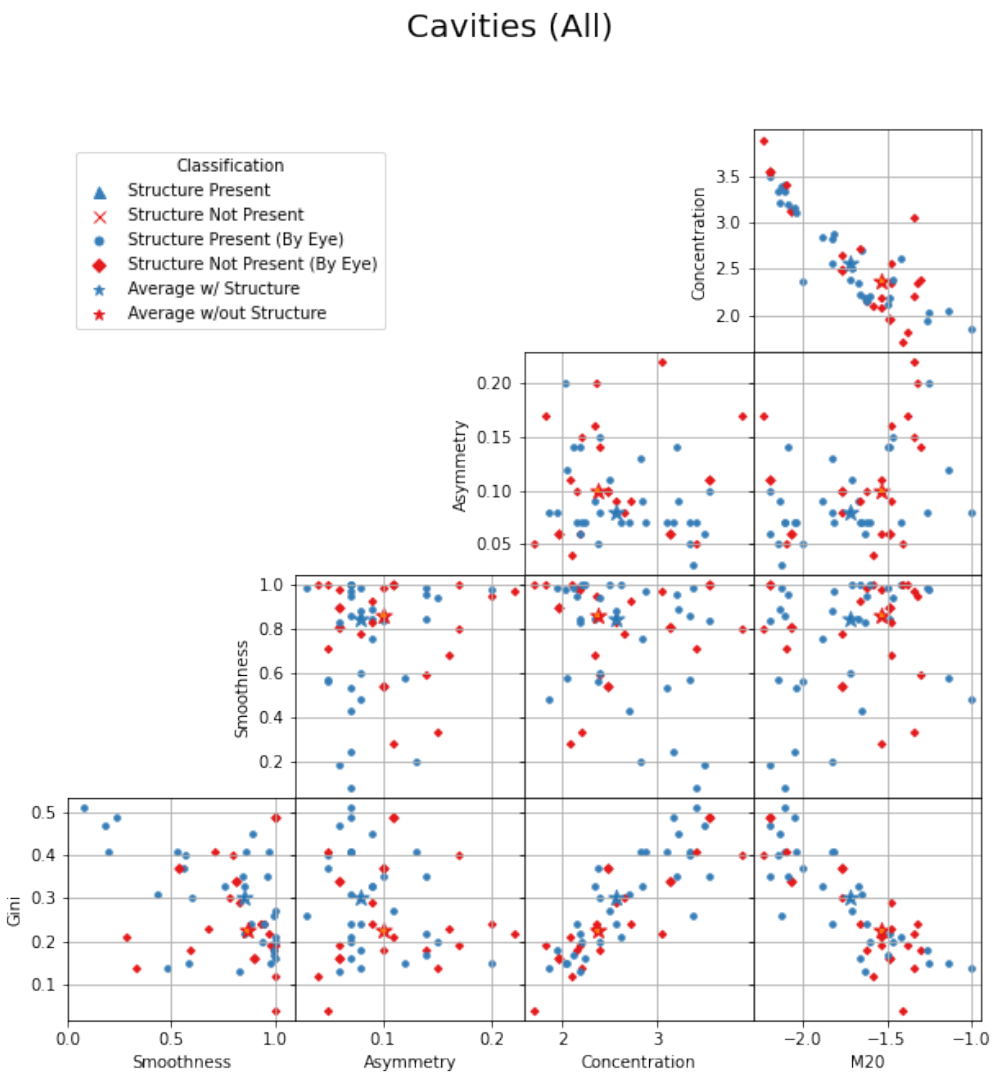

Figure 4.2: Cavities show higher G and C values and lower M_{20} and A values.

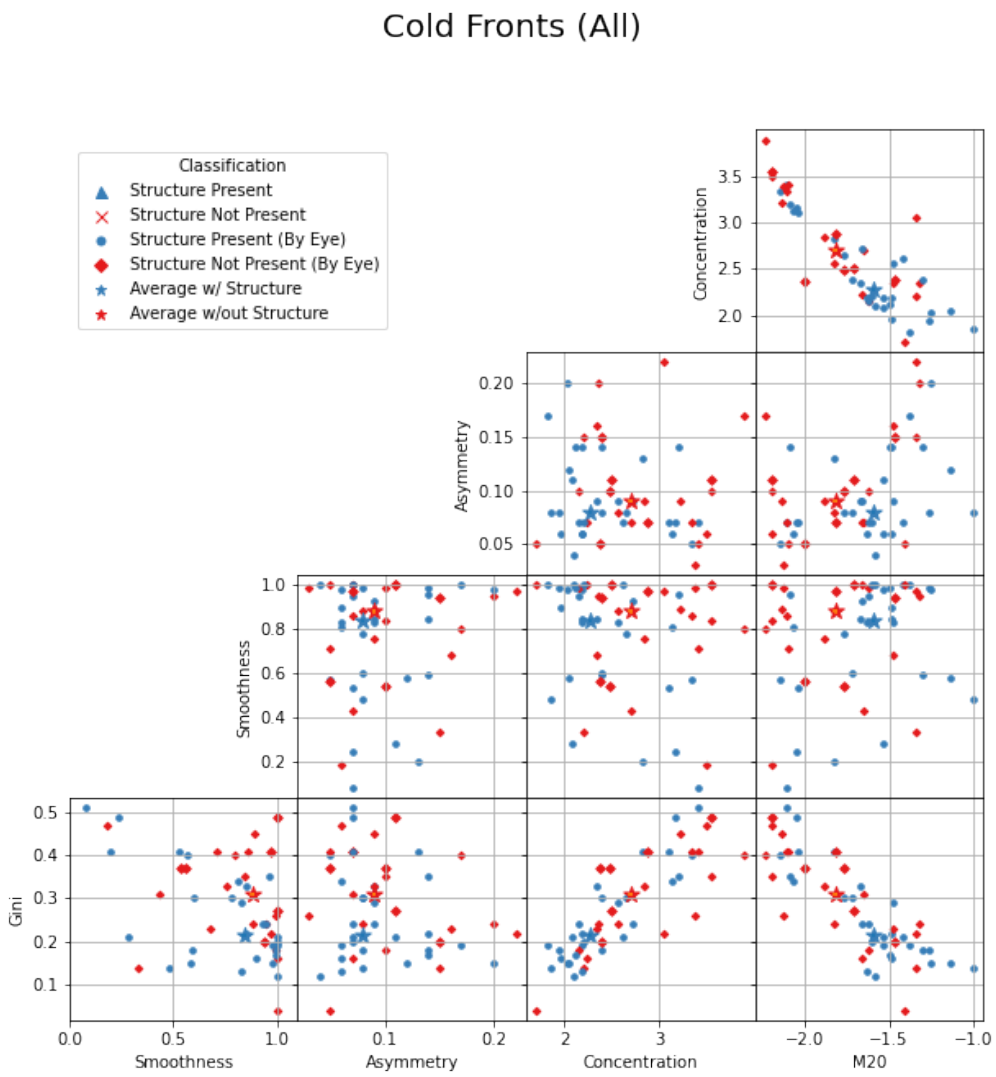

Figure 4.3: Clusters with cold fronts show higher M_{20} values and lower G and C values.

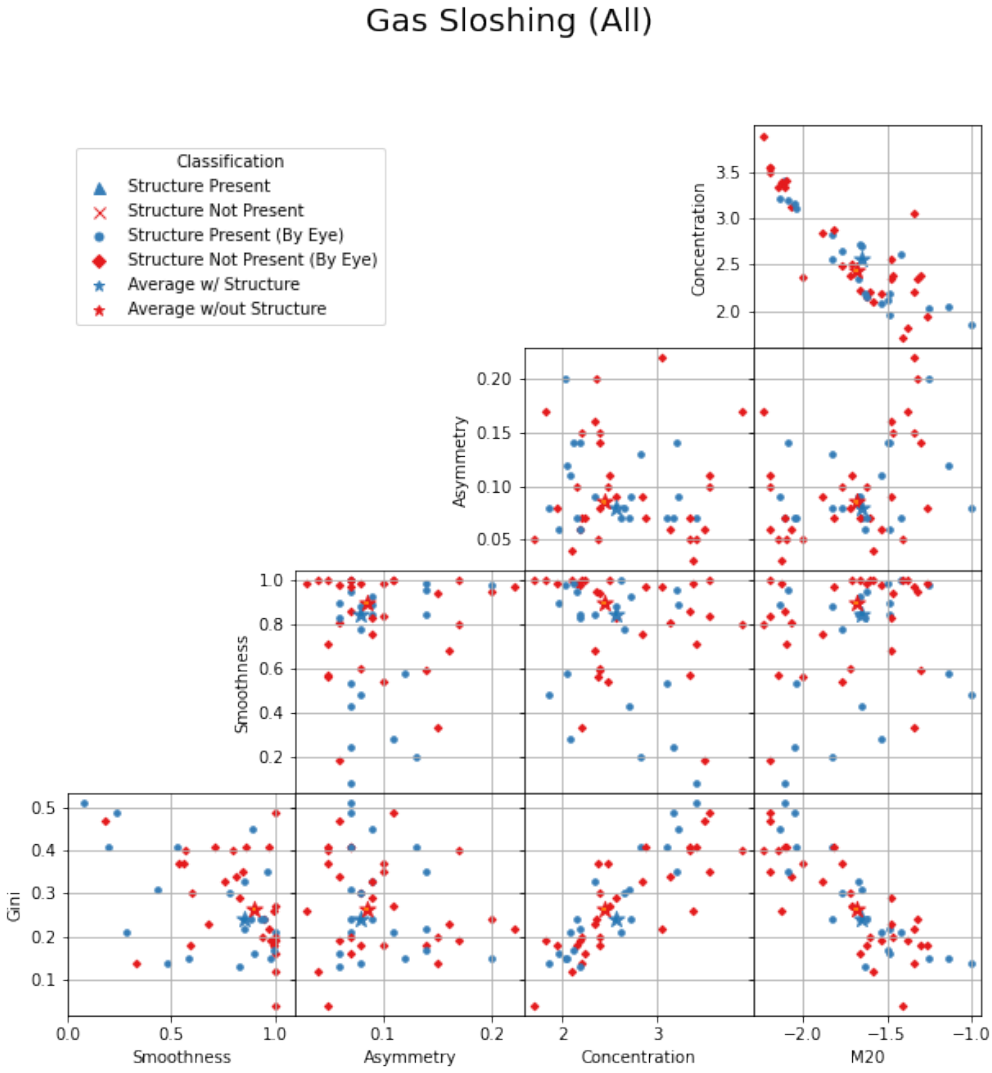

Figure 4.4: Clusters that contain sloshing gas have higher C values and lower M_{20} and G values, however the samples do not seem to be significantly different.

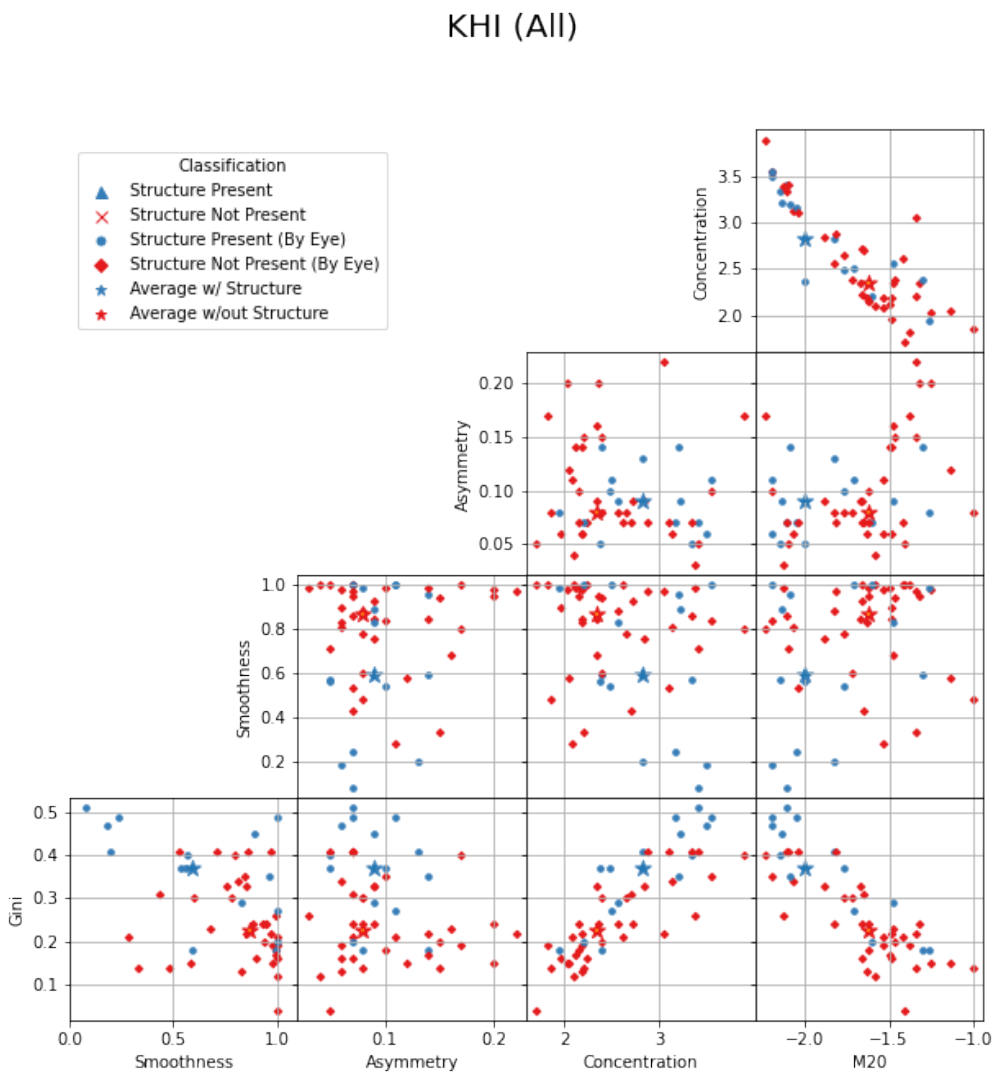

Figure 4.5: Clusters that have KHI present have lower S and M_{20} values and higher G and C values.

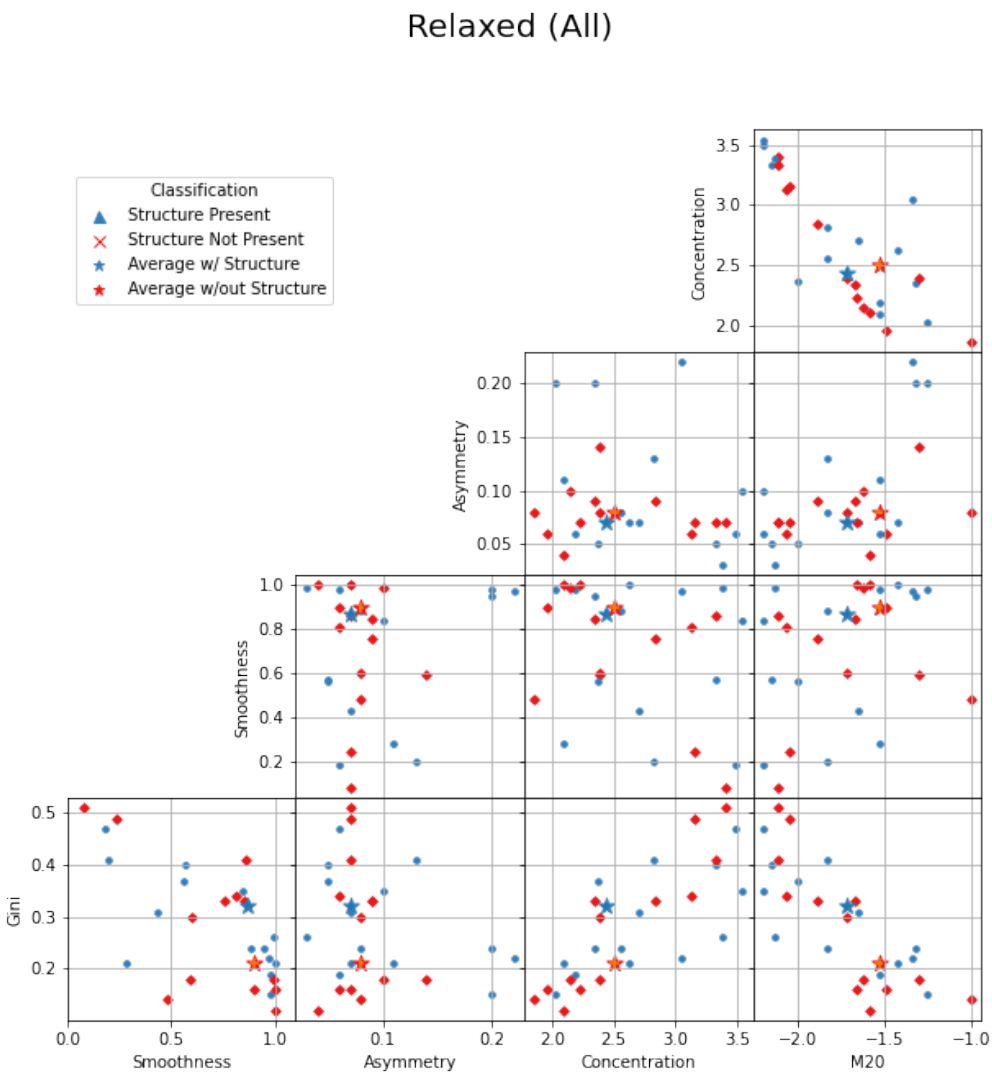

Figure 4.6: Relaxed clusters show higher G and lower M_{20} values.

5. Discussion

In previous studies, using C in combination with the Gini/M_{20} parameters provides a robust method of distinguishing relaxed clusters from disturbed clusters. This method is so robust that clusters can be predicted to be relaxed, non-relaxed and strong non-relaxed based on their C, G and M_{20} parameters (Parekh et al., 2015, 2017). Relaxed clusters have lower M_{20} values and higher C and G values. These are reflected in our results although with less statistically significant difference between the samples as calculated with the K-S test. As dynamically relaxed clusters tend to show less substructure which would generally present in an even light distribution with an increase in luminosity as distance to the centre of the cluster decreases. Our study focuses on clusters with a redshift between $0.01 < z < 0.07$ whereas Parekh et al. (2015) uses clusters ranging from $0.02 < z < 0.9$ which are separated into sub-samples of lower redshift $0.02 < z < 0.3$ and higher redshift $0.3 < z < 0.9$. We limit our redshift range to standardize our sample for the algorithm, however future study would include increased sensitivity so higher redshifted clusters may be included.

Disturbed clusters share correlations with cold fronts, gas sloshing and bow shocks. We find disturbed clusters have low G values which is also indicative of sloshing and bow shocks. Their high M_{20} values correlate with bow shocks and cold fronts. This is supported by Abell 1644, the disturbed cluster (Parekh et al., 2015) has been determined to have cold fronts and sloshing by (Johnson et al., 2010). Similarly, Abell 576 is disturbed Parekh et al. (2015) and has been shown to display signs of a cold front (Ghizzardi et al., 2010).

The results of the parameters for bow shocks and cold fronts show that they correlate. Clusters with bow shocks can be determined with high M_{20}, low G and low C. This correlates with clusters with cold fronts as they also show high M_{20}, low G and low C. As bow shocks are generally present where there is already a cold front this similarity in results makes sense. A study on the cluster MACS J0553.4-3342 (Pandge et al., 2017) which contains a cold front, finds high M_{20} and low G which supports these results.

The presence of X-ray cavities can be distinguished with high G and low M_{20} together From one study on Abell 2384 in which X-ray cavities are detected, the G value is 0.46±0.0035 (Parekh et al., 2020) which reflects well with our results. Generally, it would be expected that the S value would be higher for clusters with X-ray cavities as this shows higher clumpiness. This disparity in expectations vs reality is also present in relation to KHI. However, in Fig. 4.5 there is a very clear correlation between high S values and a lack of KHI. Unfortunately, there is not much literature in this specific area but KHI may just too subtle to detect with this method.

The Asymmetric index does not show significant difference in any of the samples. On one hand this is surprising as many of the clusters that show substructure are very asymmetric and A is used successfully used in the study of galaxy morphology (Conselice, 2014). However, in the study of cluster morphology the A index is less reliable. When classifying relaxed/disturbed clusters it is found to be dependent on the exposure time or signal-to-noise ratio (Parekh et al., 2015). Whilst there are studies on galaxies that use A and S reliably (Conselice et al., 2003; Conselice, 2006; Conselice et al., 2009), there does not seem to be conclusive evidence of these parameters being robust in the study of galaxy clusters. More commonly, C is used in combination with M_{20} and G to quantify cluster morphology. In addition, Gini/M_{20} method is found to be more reliable in the study of galaxies too (Lotz et al., 2004).

Whilst some parameters show a distinction between substructure and lack thereof, there is generally not a significant enough difference between the samples with and without structure. Various tests have been performed to try and find more significant distinction between the features with only a slight success. Firstly, improving the cropping around the clusters. This was a success as the K-S results showed more significant difference between the samples without changing the results of the parameters. Other tests include masking portions of the centre of the clusters and recalculating A and S. A larger sample of $Chandra$ and $XMM-Newton$ images could be a significant improvement in the results. This would require increasing the limits on redshift and X-ray luminosity to include a larger total sample which could need more thorough image processing to keep a consistent sample of clusters with similar resolution and exposure. However, this would be the aim of any future study as a

method that can be applied to all clusters at any redshift is the ultimate goal whereas our paper's main aim is to determine whether or not there is any correlation between cluster features and quantifiable parameters. Increasing the sample size would give rise to the opportunity to include more clusters that have the structure confirmed through literature. As we cannot be 100% certain that our "by-eye" method is accurate, replacing these clusters with those that have been confirmed to have structure present through study would provide robustness to our method. When comparing our sample split into $XMM-Newton$ and $Chandra$ clusters, the results show the same trends. We evaluate these results in Appendix C for each type of structure. This is promising as the results do not seem to change depending on telescope. This suggests the difference in resolution and depth is not an issue for our sample.

To summarise our results, there is difference in C for clusters with KHI, bow shocks, cavities and cold fronts. M_{20} shows differences in relaxed clusters and clusters with bow shocks, cavities, cold fronts and KHI. This difference is even greater when combined with G which has significant differences for relaxed, bow shock, cavity, cold front and KHI clusters. There is not a significant difference in S or A for most samples except S for KHI and A for bow shocks.

One of the greatest obstacles in classification is the reliance on human observers to classify objects such as clusters by eye or by scientific analysis. The shear magnitude of data is far too great and as such computational methods have been developed for the past few decades. The evolution of these programs and algorithms has brought forward machine learning as the most likely next step. Significant progress has been made with supervised machine learning approaches such as convolution neural networks (CNN) which have been successful in identifying galaxy morphology (Dieleman et al., 2015; Huertas-Company et al., 2015; Aniyan & Thorat, 2017; Alger et al., 2018) and supernovae types (Kessler et al., 2010; Karpenka et al., 2013; Charnock & Moss, 2017) for example. In the field of galaxy clusters there are a number of studies that use CNNs to achieve various goals such as estimating dynamical cluster masses through spectral analysis (Ho et al., 2019; Ntampaka et al., 2019; Gupta & Reichardt, 2020; Yan et al., 2020; Kodi Ramanah et al., 2021) or through weak-lensing observations (Hong et al., 2021). CNNs have been trained to identify cluster members on imaging data alone with a

purity-completeness rate of $\gtrsim 90\%$ using spectroscopic information and MUSE observations (Angora et al., 2020). This study is particularly promising as the CNN has a remarkable generalisation capability with respect to redshift which makes this an exceptionally robust method of identifying cluster members which in turn enables measurements of clusters' physical properties to be far more reliable.

Recognising and classifying clusters with CNNs is a more recent development but shows great promise for the future. CNNs are able to identify diffuse radio sources (clusters and filaments) (Gheller et al., 2018) and Sunyaev-Zel'dovich clusters (Lin et al., 2021) with varying levels of success while CNNs trained on the citizen science Zooniverse project are able to identify clusters with an accuracy of 90% (Kosiba et al., 2020). While these methods are limited to identification there is promise in the field of classification as one study is able to classify clusters as cool core (CC), weak cool core (WCC) and non-cool core (NCC) based on low-resolution mock *Chandra* images without reliance on spectral information (Su et al., 2020). The balanced accuracy of which is 92% accurate for CCs, 81% for WCCs and 83% for NCCs. Therefore, providing more accurate classifications than traditional methods such as using central gas densities and surface brightness concentrations. Future studies could include training a CNN with the quantifiable parameters we use to correlate with structure in order to predict whether a cluster will have a specific feature based on its CAS, G and M_{20} results. This could be combined with other quantifiable parameters such as ellipticity, Gini of the second-order moment, cuspiness or power ratios to build a more rigorous training scheme for the CNN. In fact, a similar approach is attempted by Green et al. (2019) in a study using *Chandra* and *eROSITA* mock X-ray images to train a random forest regressor to predict cluster masses from X-ray luminosities and morphological parameters such as A, S, M_{20}, power ratios and ellipticity, among others. They use two series of images, ideal *Chandra* mock images and realistic-condition *eROSITA* mocks in order to evaluate the potential improvement in mass estimation of lower resolution, real cluster images. While there is some underestimate of mass in the high-mass tail of the halo mass function, they suggest this will improve when the model is trained with a larger sample of clusters that is consistent across a complete mass range. In conclusion, this is a promising method for future

study with a larger sample of images to potentially train a CNN or other machine learning algorithm.

Bibliography

Abell G. O., 1958, ApJS, 3, 211

Abell G. O., 1965, ARA&A, 3, 1

Abraham R. G., van den Bergh S., Nair P., 2003, ApJ, 588, 218

Alger M. J., et al., 2018, MNRAS, 478, 5547

Allen S. W., Schmidt R. W., Ebeling H., Fabian A. C., van Speybroeck L., 2004, MNRAS, 353, 457

Angora G., et al., 2020, A&A, 643, A177

Aniyan A. K., Thorat K., 2017, ApJS, 230, 20

Ascasibar Y., Markevitch M., 2006, ApJ, 650, 102

Bautz L. P., Morgan W. W., 1970, ApJL, 162, L149

Berlok T., Pfrommer C., 2019, MNRAS, 485, 908

Bîrzan L., Rafferty D. A., McNamara B. R., Wise M. W., Nulsen P. E. J., 2004, ApJ, 607, 800

Blanton E. L., Sarazin C. L., McNamara B. R., Wise M. W., 2001, ApJL, 558, L15

Blumenthal G. R., Faber S. M., Primack J. R., Rees M. J., 1984, Nature, 311, 517

Boehringer H., Voges W., Fabian A. C., Edge A. C., Neumann D. M., 1993, MNRAS, 264, L25

Bond J. R., Kofman L., Pogosyan D., 1996, Nature, 380, 603

Borgani S., Kravtsov A., 2011, Advanced Science Letters, 4, 204

Breuer J. P., Werner N., Mernier F., Mroczkowski T., Simionescu A., Clarke T. E., ZuHone J. A., Di Mascolo L., 2020, MNRAS, 495, 5014

Buote D. A., 2002, X-Ray Observations of Cluster Mergers. Springer Netherlands, p. 79–107, doi:10.1007/0-306-48096-4_3, http://dx.doi.org/10.1007/0-306-48096-4_3

Buote D. A., Tsai J. C., 1995, ApJ, 452, 522

Cautun M., van de Weygaert R., Jones B. J. T., Frenk C. S., 2014, MNRAS, 441, 2923

Charnock T., Moss A., 2017, ApJL, 837, L28

Churazov E., Forman W., Jones C., Böhringer H., 2003, ApJ, 590, 225

Churazov E., Khabibullin I., Lyskova N., Sunyaev R., Bykov A. M., 2021, A&A, 651, A41

Clarke T. E., Enßlin T., Finoguenov A., Intema H., Pfrommer C., van Weeren R., Röttgering H., Oonk R., 2011, , 82, 547

Clowe D., Gonzalez A., Markevitch M., 2004, ApJL, 604, 596–603

Clowe D., Bradač M., Gonzalez A. H., Markevitch M., Randall S. W., Jones C., Zaritsky D., 2006, ApJL, 648, L109

Cole S., Lacey C., 1996, MNRAS, 281, 716

Conselice C. J., 2003, ApJS, 147, 1

Conselice C. J., 2006, MNRAS, 373, 1389

Conselice C. J., 2014, ARA&A, 52, 291

Conselice C. J., Bershady M. A., Dickinson M., Papovich C., 2003, AJ, 126, 1183

Conselice C. J., Yang C., Bluck A. F. L., 2009, MNRAS, 394, 1956

Crone M. M., Evrard A. E., Richstone D. O., 1994, ApJ, 434, 402

David L. P., Nulsen P. E. J., McNamara B. R., Forman W., Jones C., Ponman T., Robertson B., Wise M., 2001, ApJ, 557, 546

Davis M., Efstathiou G., Frenk C. S., White S. D. M., 1985, ApJ, 292, 371

Dieleman S., Willett K. W., Dambre J., 2015, MNRAS, 450, 1441

Dupke R., White Raymond E. I., 2003, ApJL, 583, L13

Ebeling H., White D. A., Rangarajan F. V. N., 2006, MNRAS, 368, 65

Fabian A. C., 1994, ARA&A, 32, 277

Fabian A. C., Nulsen P. E. J., 1977, MNRAS, 180, 479

Fabian A. C., Crawford C. S., Edge A. C., Mushotzky R. F., 1994, MNRAS, 267, 779

Fabian A. C., et al., 2000, MNRAS, 318, L65

Fabian A. C., Sanders J. S., Ettori S., Taylor G. B., Allen S. W., Crawford C. S., Iwasawa K., Johnstone R. M., 2001, MNRAS, 321, L33

Fasano G., Franceschini A., 1987, , 225, 155

Ferrari C., Benoist C., Maurogordato S., Cappi A., Slezak E., 2005, A&A, 430, 19

Fort S., 2017, arXiv e-prints, p. arXiv:1712.00523

Fujita Y., Sarazin C. L., Kempner J. C., Rudnick L., Slee O. B., Roy A. L., Andernach H., Ehle M., 2002, ApJ, 575, 764

Geller M. J., Huchra J. P., 1989, Science, 246, 897

Geller M. J., Diaferio A., Rines K. J., Serra A. L., 2013, ApJ, 764, 58

Gheller C., Vazza F., Bonafede A., 2018, MNRAS, 480, 3749

Ghirardini V., et al., 2022, A&A, 661, A12

Ghizzardi S., Rossetti M., Molendi S., 2010, A&A, 516, A32

Giacconi R., et al., 2001, ApJ, 551, 624

Green S. B., Ntampaka M., Nagai D., Lovisari L., Dolag K., Eckert D., ZuHone J. A., 2019, ApJ, 884, 33

Grubbs F. E., 1950, Annals of Mathematics Studies, 21, 27

Gupta N., Reichardt C. L., 2020, ApJ, 900, 110

Hlavacek-Larrondo J., et al., 2015, ApJ, 805, 35

Ho M., Rau M. M., Ntampaka M., Farahi A., Trac H., Póczos B., 2019, ApJ, 887, 25

Holwerda B. W., Pirzkal N., Cox T. J., de Blok W. J. G., Weniger J., Bouchard A., Blyth S. L., van der Heyden K. J., 2011, MNRAS, 416, 2426

Hong S. E., Park S., Jee M. J., Bak D., Cha S., 2021, arXiv e-prints, p. arXiv:2102.05403

Hoyos C., et al., 2012, MNRAS, 419, 2703

Hradecky V., Jones C., Donnelly R. H., Djorgovski S. G., Gal R. R., Odewahn S. C., 2000, ApJ, 543, 521

Hudson D. S., Mittal R., Reiprich T. H., Nulsen P. E. J., Andernach H., Sarazin C. L., 2010, A&A, 513, A37

Huertas-Company M., et al., 2015, ApJS, 221, 8

Ichinohe Y., Simionescu A., Werner N., Fabian A. C., Takahashi T., 2019, MNRAS, 483, 1744

Ichinohe Y., Simionescu A., Werner N., Markevitch M., Wang Q. H. S., 2021, MNRAS, 504, 2800

Johnson R. E., Markevitch M., Wegner G. A., Jones C., Forman W. R., 2010, ApJ, 710, 1776

Jones C., Forman W., 1992, in Fabian A. C., ed., NATO Advanced Study Institute (ASI) Series C Vol. 366, Clusters and Superclusters of Galaxies. p. 49, doi:10.1007/978-94-011-2482-9_4

Kapferer W., et al., 2006, A&A, 447, 827

Karpenka N. V., Feroz F., Hobson M. P., 2013, MNRAS, 429, 1278

Kessler R., et al., 2010, PASP, 122, 1415

Kodi Ramanah D., Wojtak R., Arendse N., 2021, MNRAS, 501, 4080

Kosiba M., et al., 2020, MNRAS, 496, 4141

Laganá T. F., Durret F., Lopes P. A. A., 2019, MNRAS, 484, 2807

Lee Y., Rey S.-C., Hilker M., Sheen Y.-K., Yi S. K., 2016, ApJ, 822, 92

Lin Y.-T., Mohr J. J., 2004, ApJ, 617, 879

Lin Z., Huang N., Avestruz C., Wu W. L. K., Trivedi S., Caldeira J., Nord B., 2021, MNRAS,

Lorenz M. O., 1905, Publications of the American Statistical Association, 9, 209

Lotz J. M., Primack J., Madau P., 2004, AJ, 128, 163

Machacek M., Dosaj A., Forman W., Jones C., Markevitch M., Vikhlinin A., Warmflash A., Kraft R., 2005, ApJ, 621, 663

Marini F., et al., 2004, MNRAS, 353, 1219

Markevitch M., Vikhlinin A., 2007, , 443, 1

Markevitch M., et al., 2000, ApJ, 541, 542

Markevitch M., Vikhlinin A., Mazzotta P., 2001, ApJL, 562, L153

Markevitch M., Gonzalez A. H., David L., Vikhlinin A., Murray S., Forman W., Jones C., Tucker W., 2002, ApJL, 567, L27

Markevitch M., et al., 2003, ApJL, 586, L19

Markevitch M., Gonzalez A. H., Clowe D., Vikhlinin A., Forman W., Jones C., Murray S., Tucker W., 2004, ApJ, 606, 819

Markevitch M., Govoni F., Brunetti G., Jerius D., 2005, ApJ, 627, 733

Mathews W. G., Brighenti F., 2007, ApJ, 660, 1137

Mazzotta P., Markevitch M., Vikhlinin A., Forman W. R., David L. P., van Speybroeck L., 2001, ApJ, 555, 205

McCleary J., dell'Antonio I., Huwe P., 2015, ApJ, 805, 40

McNamara B. R., et al., 2000, ApJL, 534, L135

Ntampaka M., et al., 2019, ApJ, 876, 82

Nulsen P. E. J., 1982, MNRAS, 198, 1007

Nulsen P. E. J., et al., 2013, ApJ, 775, 117

Owers M. S., Couch W. J., Nulsen P. E. J., 2009, ApJ, 693, 901

Pandge M. B., et al., 2017, MNRAS, 472, 2042

Parekh V., van der Heyden K., Ferrari C., Angus G., Holwerda B., 2015, A&A, 575, A127

Parekh V., Dwarakanath K. S., Kale R., Intema H., 2017, MNRAS, 464, 2752

Parekh V., Laganá T. F., Thorat K., van der Heyden K., Iqbal A., Durret F., 2020, MNRAS, 491, 2605

Pasini T., Gitti M., Brighenti F., O'Sullivan E., Gastaldello F., Temi P., Hamer S. L., 2021, ApJ, 911, 66

Peebles P. J. E., 1982, ApJL, 263, L1

Pogosyan D., Bond J. R., Kofman L., Wadsley J., 1998, in Colombi S., Mellier Y., Raban B., eds, Vol. 14, Wide Field Surveys in Cosmology. p. 61 (arXiv:astro-ph/9810072)

Proust D., Capelato H. V., Hickel G., Sodré L. J., Lima Neto G. B., Cuevas H., 2003, A&A, 407, 31

Randall S. W., Clarke T. E., Nulsen P. E. J., Owers M. S., Sarazin C. L., Forman W. R., Murray S. S., 2010, ApJ, 722, 825

Rasia E., Meneghetti M., Ettori S., 2013, The Astronomical Review, 8, 40

Richstone D., Loeb A., Turner E. L., 1992, ApJ, 393, 477

Roediger E., Brüggen M., Simionescu A., Böhringer H., Churazov E., Forman W. R., 2011, MNRAS, 413, 2057

Roediger E., Lovisari L., Dupke R., Ghizzardi S., Brüggen M., Kraft R. P., Machacek M. E., 2012, MNRAS, 420, 3632

Roediger E., Kraft R. P., Nulsen P., Churazov E., Forman W., Brüggen M., Kokotanekova R., 2013a, MNRAS, 436, 1721

Roediger E., Kraft R. P., Forman W. R., Nulsen P. E. J., Churazov E., 2013b, ApJ, 764, 60

Roettiger K., Loken C., Burns J. O., 1997, ApJS, 109, 307

Sadat R., Blanchard A., Kneib J. P., Mathez G., Madore B., Mazzarella J. M., 2004, A&A, 424, 1097

Sanders J. S., Fabian A. C., Taylor G. B., 2005, MNRAS, 356, 1022

Sarazin C. L., 1986, Reviews of Modern Physics, 58, 1

Sarazin C. L., Kempner J. C., 2000, ApJ, 533, 73

Sauvageot J. L., Belsole E., Pratt G. W., 2005, A&A, 444, 673

Scarlata C., et al., 2007, ApJS, 172, 406

Shin J., Woo J.-H., Mulchaey J. S., 2016, ApJS, 227, 31

Sijacki D., Pfrommer C., Springel V., Enßlin T. A., 2008, MNRAS, 387, 1403

Sousbie T., 2011, MNRAS, 414, 350

Su Y., et al., 2020, MNRAS, 498, 5620

Sun M., Murray S. S., Markevitch M., Vikhlinin A., 2002, ApJ, 565, 867

Takizawa M., 1999, ApJ, 520, 514

Vikhlinin A., Markevitch M., Murray S. S., 2001a, ApJL, 549, L47

Vikhlinin A., Markevitch M., Murray S. S., 2001b, ApJ, 551, 160

Wang Q. H. S., Markevitch M., 2018, ApJ, 868, 45

Wen Z. L., Han J. L., 2013, MNRAS, 436, 275

Werner N., et al., 2016, MNRAS, 460, 2752

White S. D. M., Navarro J. F., Evrard A. E., Frenk C. S., 1993, Nature, 366, 429

Yan Z., Mead A. J., Van Waerbeke L., Hinshaw G., McCarthy I. G., 2020, MNRAS, 499, 3445

Yu H., Serra A. L., Diaferio A., Baldi M., 2015, ApJ, 810, 37

Yu H., Diaferio A., Agulli I., Aguerri J. A. L., Tozzi P., 2016, ApJ, 831, 156

Zamojski M. A., et al., 2007, ApJS, 172, 468

ZuHone J. A., Markevitch M., Johnson R. E., 2010, ApJ, 717, 908

Zuhone J. A., Roediger E., 2016, Journal of Plasma Physics, 82, 535820301

Zwicky F., 1933, Helvetica Physica Acta, 6, 110

A. Appendix: Gallery of Clusters

We present a gallery of our clusters, separated into the respective observing telescopes. $Chandra$ images are displayed in Fig. A.1 and $XMM-Newton$ clusters are shown in Fig. A.2 and Fig. A.3. Please refer to Table 2.1 for apparent structure.

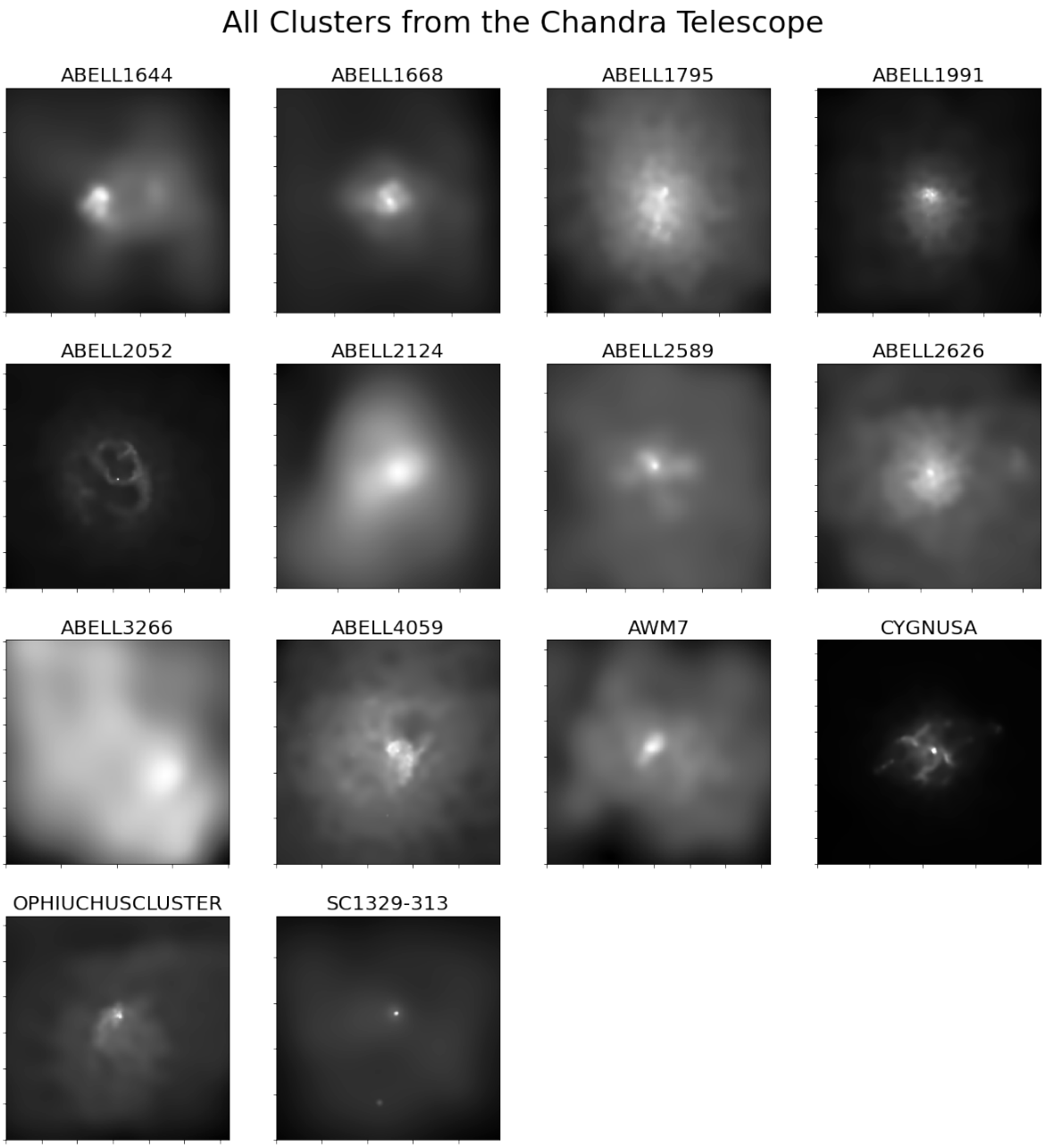

Figure A.1: *Chandra* images used to show structure of clusters. Prominent clusters include Abell 1644 that has sloshing gas and a cold front and Abell 2052 has two large X-ray cavities. Images are filtered within an energy band range of 0.5-3keV, then adaptively smoothed and cropped to a scale of ~100kpc, the full process is discussed in more detail in Section 2.2.

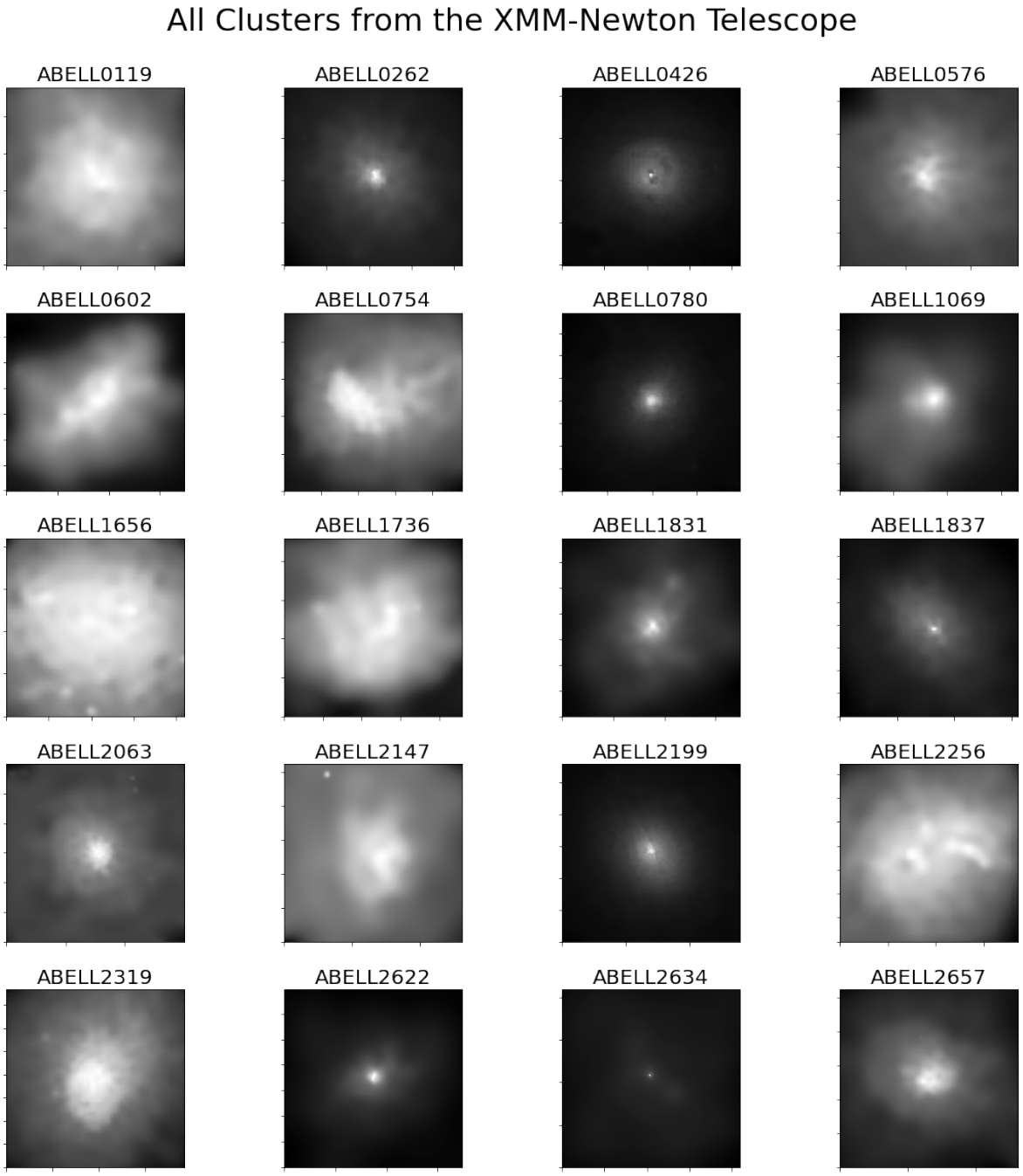

Figure A.2: *XMM − Newton* images used to show structure of clusters. Prominent clusters include Abell 754 that shows a cold front and Abell 426 that shows X-ray cavities. Images are filtered within an energy band range of 0.5-3keV, then adaptively smoothed and cropped to a scale of ~100kpc, the full process is discussed in more detail in Section 2.2.

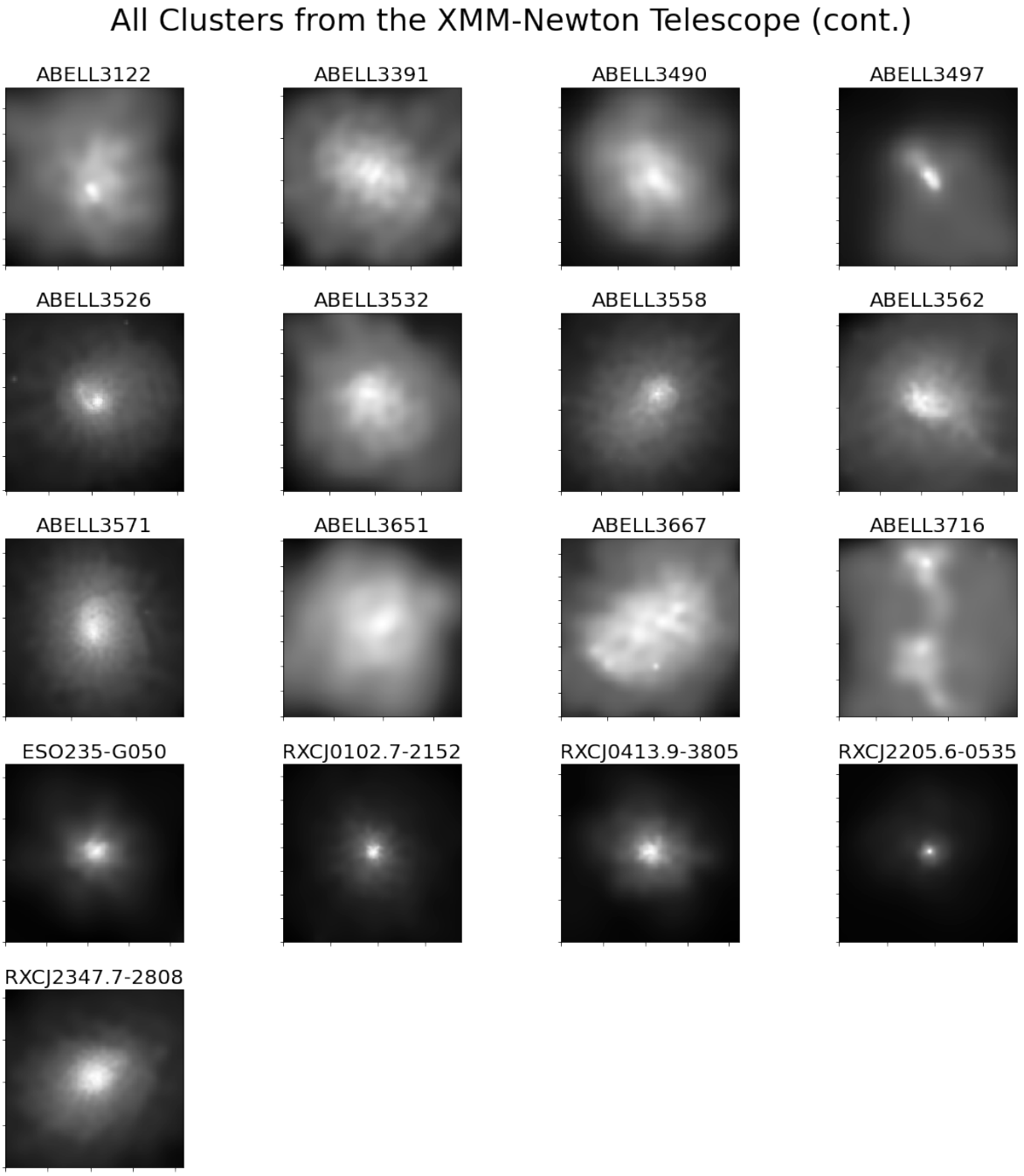

Figure A.3: $XMM-Newton$ images used to show structure of clusters. Prominent clusters include Abell 3526 that shows a cold front and Abell 3571 that shows cavities. Images are filtered within an energy band range of 0.5-3keV, then adaptively smoothed and cropped to a scale of ~100kpc, the full process is discussed in more detail in Section 2.2.

B. Appendix: Results by Cluster

In this appendix we present Table B.1 that shows the results of the parameters for each cluster, their ObsID and exposure times. We display the median values for each type of structure present alongside the standard errors for said classification in Table B.2.

Cluster	ObsID	Exposure (s)	C	A	S	G	M
A0119	505211001	12110	1.96	0.06	0.9	0.16	-1.49
A0262	109980101	23891	3.33	0.05	0.57	0.4	-2.15
A0426	85110101	53597	3.4	0.07	0.08	0.51	-2.11
A0576	205070301	18353	3.13	0.06	0.81	0.34	-2.07
A0602	761112401	10618	2.35	0.2	0.95	0.24	-1.32
A0754	136740101	14417	2.39	0.14	0.59	0.18	-1.3
A0780	504260101	101228	3.49	0.06	0.18	0.47	-2.2
A1069	720251801	6645	3.05	0.22	0.97	0.22	-1.34
A1644	2206	18713	2.62	0.07	1.0	0.21	-1.42
A1656	153750101	25194	2.09	0.11	0.28	0.21	-1.53
A1668	12877	9977	3.38	0.03	0.99	0.26	-2.13
A1736	300210301	8707	2.03	0.2	0.98	0.15	-1.25
A1795	10900	15823	2.34	0.09	0.85	0.33	-1.67
A1831	827030901	16299	2.84	0.09	0.76	0.33	-1.89
A1837	109910101	49013	2.39	0.08	0.6	0.3	-1.72
A1991	3193	38304	3.33	0.07	0.86	0.41	-2.11
A2052	5807	126950	2.7	0.07	0.43	0.31	-1.65
A2063	200120401	18847	2.37	0.05	0.56	0.37	-2.0
A2124	3238	19351	2.1	0.04	1.0	0.12	-1.58
A2147	300350301	5067	2.19	0.06	0.98	0.19	-1.53

Table B.1 continued from previous page

Cluster	ObsID	Exposure (s)	C	A	S	G	M
A2199	723801201	54119	3.16	0.07	0.24	0.49	-2.05
A2256	112500201	16819	1.86	0.08	0.48	0.14	-1.0
A2319	600040101	57814	2.82	0.13	0.2	0.41	-1.83
A2589	7340	14908	2.23	0.07	1.0	0.16	-1.66
A2622	765020701	22620	3.54	0.1	0.84	0.35	-2.2
A2626	16136	110848	2.56	0.08	0.88	0.24	-1.83
A2634	800761501	8494	2.15	0.1	0.99	0.18	-1.62
A2657	300210601	15459	2.65	0.08	0.78	0.3	-1.77
A3122	720253201	25496	2.19	0.14	0.85	0.22	-1.49
A3266	899	29752	1.82	0.17	1.0	0.19	-1.38
A3391	505210401	27152	2.21	0.07	1.0	0.2	-1.6
A3490	677181601	8845	2.34	0.16	0.68	0.23	-1.48
A3497	761112801	9932	2.72	0.09	0.93	0.24	-1.66
A3526	46340101	47141	3.2	0.14	0.96	0.35	-2.09
A3532	30140301	15732	2.39	0.15	0.94	0.2	-1.47
A3558	107260101	43995	2.56	0.09	0.83	0.29	-1.48
A3562	105261301	42232	2.5	0.11	1.0	0.27	-1.71
A3571	86950201	32814	2.48	0.1	0.54	0.37	-1.77
A3651	677182001	7230	2.21	0.15	0.33	0.14	-1.34
A3667	513	44838	1.95	0.08	0.99	0.18	-1.26
A3716	692930101	22388	2.05	0.12	0.58	0.15	-1.13
A4059	5785	92121	2.15	0.07	0.95	0.24	-1.62
AWM7	908	47853	2.18	0.06	0.83	0.13	-1.63
CYGNUSA	360	34719	2.87	0.07	0.97	0.41	-1.82
ESO235	765000101	12711	3.41	0.05	0.71	0.41	-2.1
OPHIUCHU	3200	50532	2.11	0.14	0.99	0.17	-1.5
RXCJ0102	144310101	23376	3.22	0.09	0.89	0.45	-2.14

Table B.1 continued from previous page

Cluster	ObsID	Exposure (s)	C	A	S	G	M
RXCJ0413	720251501	13091	3.1	0.07	0.53	0.41	-2.04
RXCJ2205	720251201	6193	3.89	0.17	0.8	0.4	-2.24
RXCJ2347	204460101	29663	3.54	0.11	1.0	0.49	-2.2
SC1329-313	4166	19372	1.71	0.05	1.0	0.04	-1.41

Table B.1: Clusters with their ObsID, exposure time and results for the CAS, G and M_{20} parameters.

Cavities	Present	Not Present
Concentration	2.56 ± 0.017	2.37 ± 0.029
Asymmetry	0.08 ± 0.001	0.1 ± 0.003
Smoothness	0.85 ± 0.009	0.865 ± 0.011
Gini	0.3 ± 0.004	0.225 ± 0.005
M20	-1.72 ± 0.011	-1.53 ± 0.015
Cold Fronts	**Present**	**Not Present**
Concentration	2.275 ± 0.017	2.7 ± 0.025
Asymmetry	0.08 ± 0.001	0.09 ± 0.002
Smoothness	0.84 ± 0.01	0.88 ± 0.01
Gini	0.215 ± 0.004	0.31 ± 0.005
M20	-1.59 ± 0.011	-1.82 ± 0.014
Bow Shocks	**Present**	**Not Present**
Concentration	2.29 ± 0.043	2.56 ± 0.014
Asymmetry	0.08 ± 0.003	0.09 ± 0.001
Smoothness	0.92 ± 0.031	0.85 ± 0.006
Gini	0.2 ± 0.01	0.29 ± 0.003

Table B.2 continued from previous page

M20	-1.53 ± 0.03	-1.67 ± 0.008
Gas Sloshing	Present	Not Present
Concentration	2.56 ± 0.022	2.435 ± 0.019
Asymmetry	0.08 ± 0.002	0.085 ± 0.002
Smoothness	0.85 ± 0.014	0.9 ± 0.007
Gini	0.24 ± 0.006	0.265 ± 0.004
M20	-1.65 ± 0.015	-1.685 ± 0.011
KHI	Present	Not Present
Concentration	2.82 ± 0.033	2.345 ± 0.015
Asymmetry	0.09 ± 0.002	0.08 ± 0.001
Smoothness	0.59 ± 0.022	0.87 ± 0.006
Gini	0.37 ± 0.007	0.225 ± 0.003
M20	-2.0 ± 0.021	-1.62 ± 0.008
Relaxed	Present	Not Present
Concentration	2.435 ± 0.035	2.5 ± 0.038
Asymmetry	0.07 ± 0.003	0.08 ± 0.002
Smoothness	0.87 ± 0.018	0.9 ± 0.022
Gini	0.32 ± 0.008	0.21 ± 0.009
M20	-1.72 ± 0.02	-1.53 ± 0.026

Table B.2: Each type of structure has a median value for whether or not it is present, with a standard error presented for each parameter.

C. Appendix: Results Separated By Telescope

In this appendix we present our results separated by telescope to determine if our correlations are affected by resolution. Fig. C.1-Fig. C.6 are results for clusters observed with the $Chandra$ telescope and Fig. C.12 - Fig. C.7 are results for clusters observed with the $XMM-Newton$ telescope. Each plot has well-known clusters labelled and averages shown.

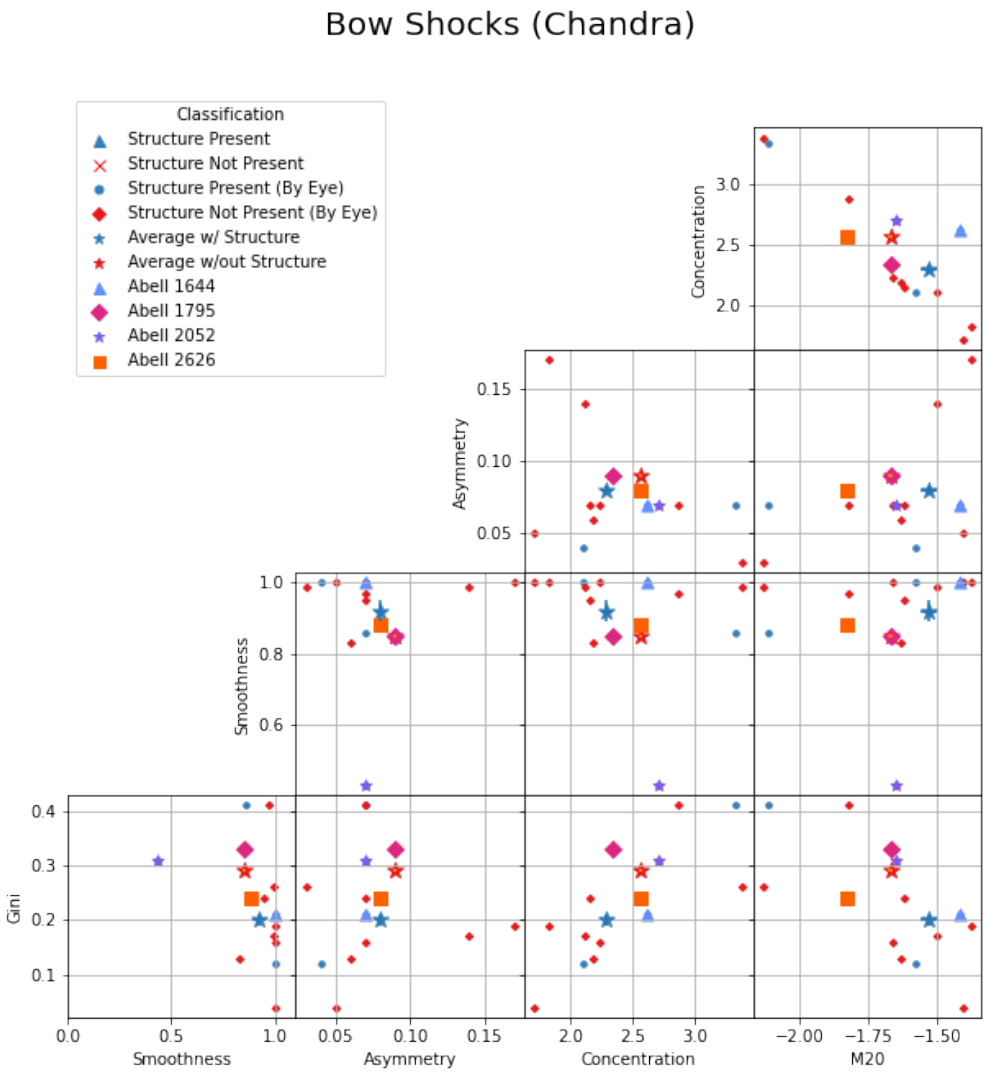

Figure C.1: Bow shocks have slight differences between the parameters M_{20}, G and C in which clusters with bow shocks have higher M_{20}, and lower G and C values. Clusters of note are Abell 1644 that has a higher M_{20} value, a confirmed cold front and may have a bow shock and Abell 1795 that has a low G value and no apparent bow shock.

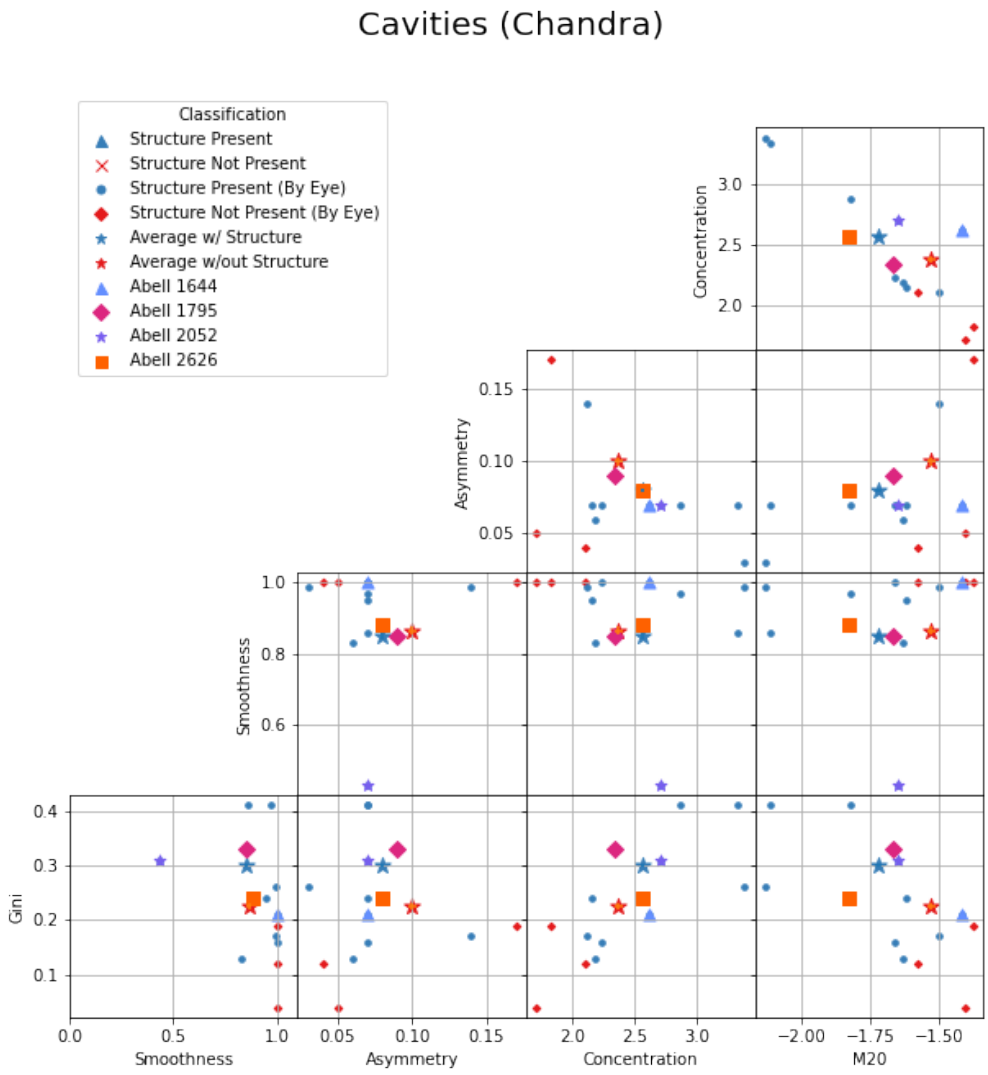

Figure C.2: Cavities show higher G and C values but lower M_{20} values. Abell 2052 has a very low S value which is unexpected because it has very prominent X-ray cavities.

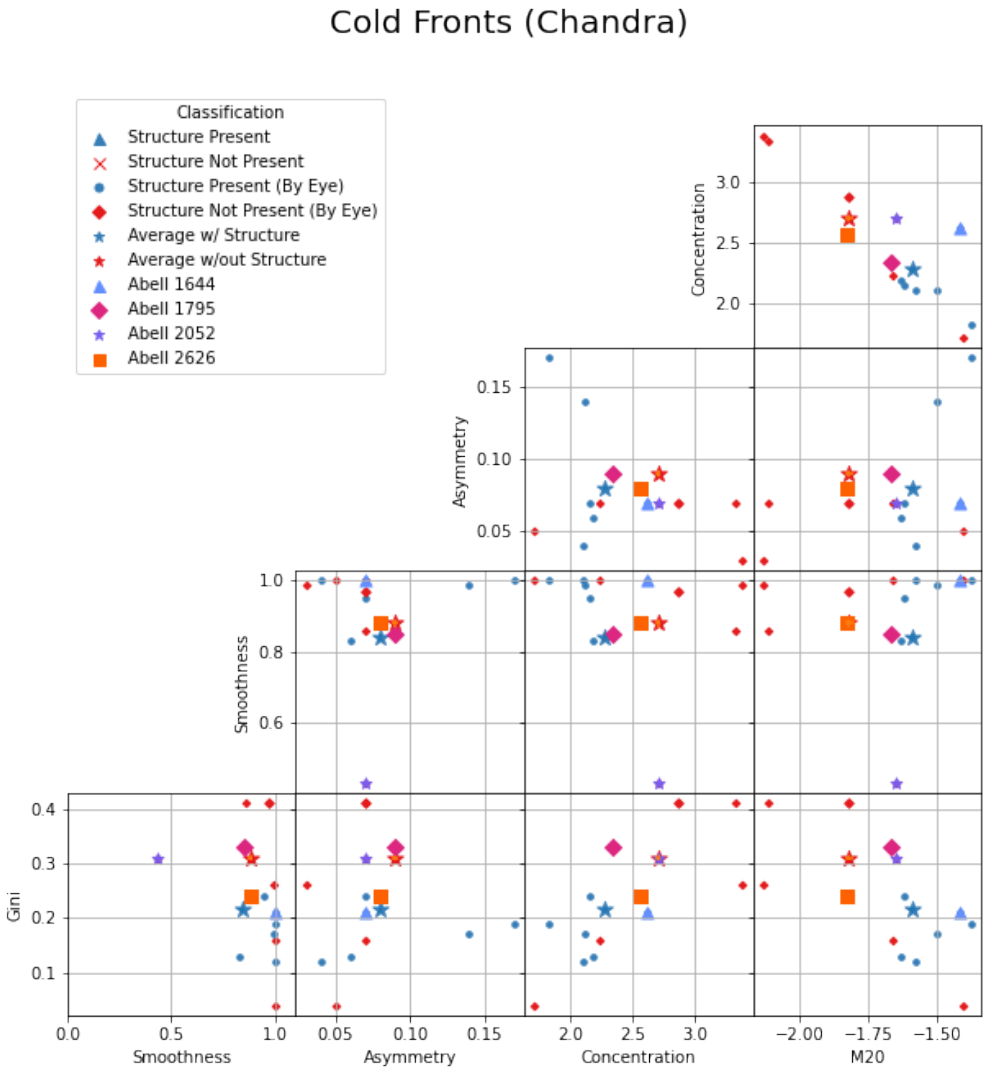

Figure C.3: Clusters with cold fronts show higher M_{20} values and lower G and C values. This is consistent with the well-known clusters as they all have cold fronts and follow this trend.

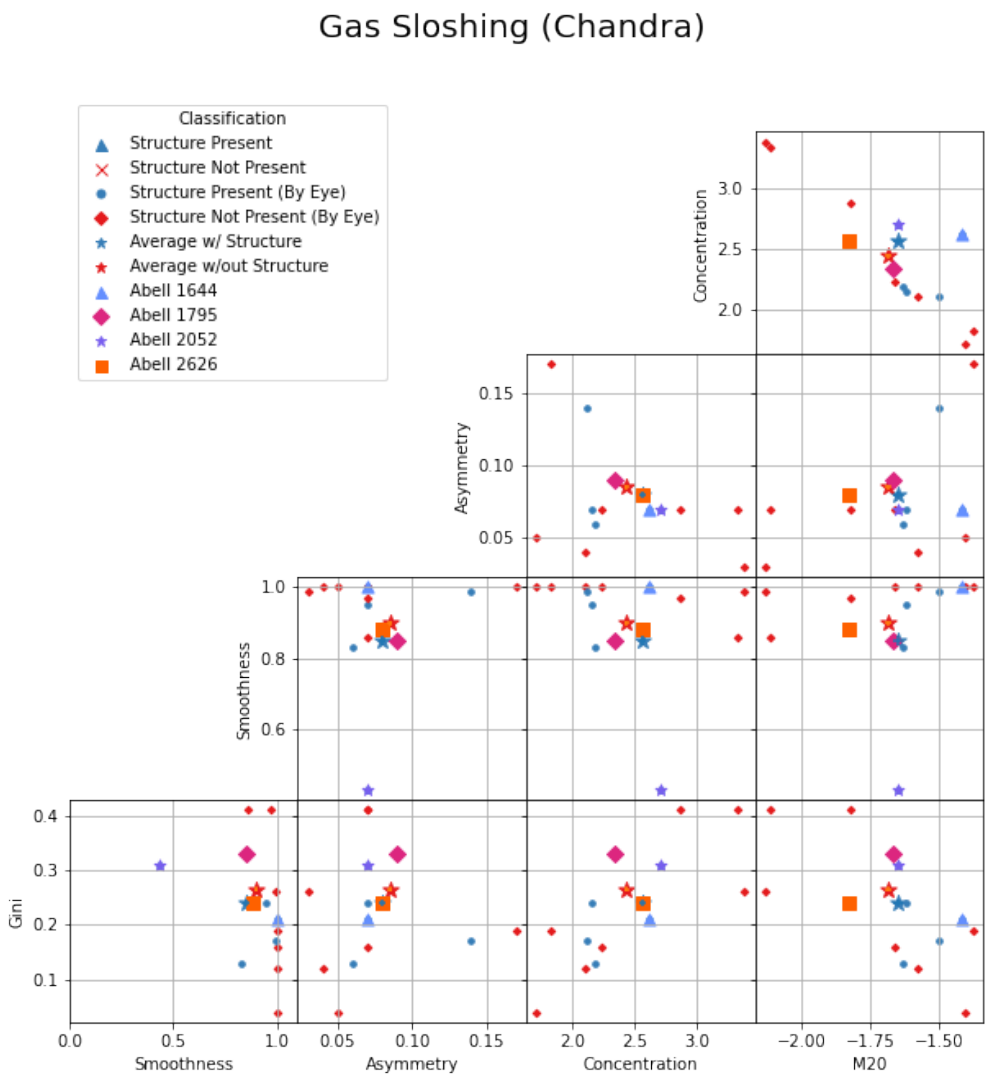

Figure C.4: Clusters that contain sloshing gas have very slightly lower G and M_{20} values. However, we would argue that the samples are indistinguishable. This shows with the well-known clusters as they all have potential or confirmed gas sloshing but they show no real trend.

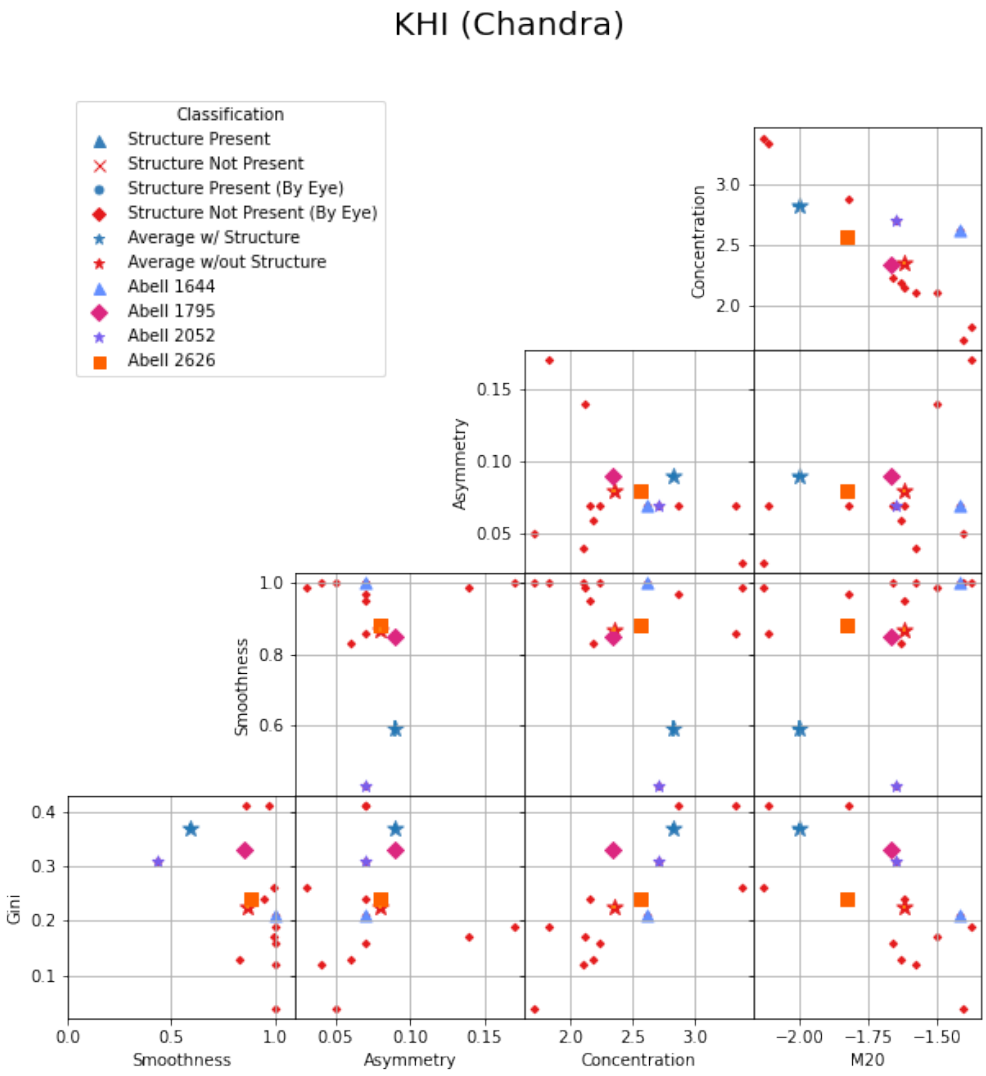

Figure C.5: Clusters that have KHI present have higher C and G values but lower M_{20} and S values. None of the well-known clusters have KHI confirmed by literature but by-eye, Abell 2052 and 2626 could potentially have KHI present however, their results do not show that they follow this trend.

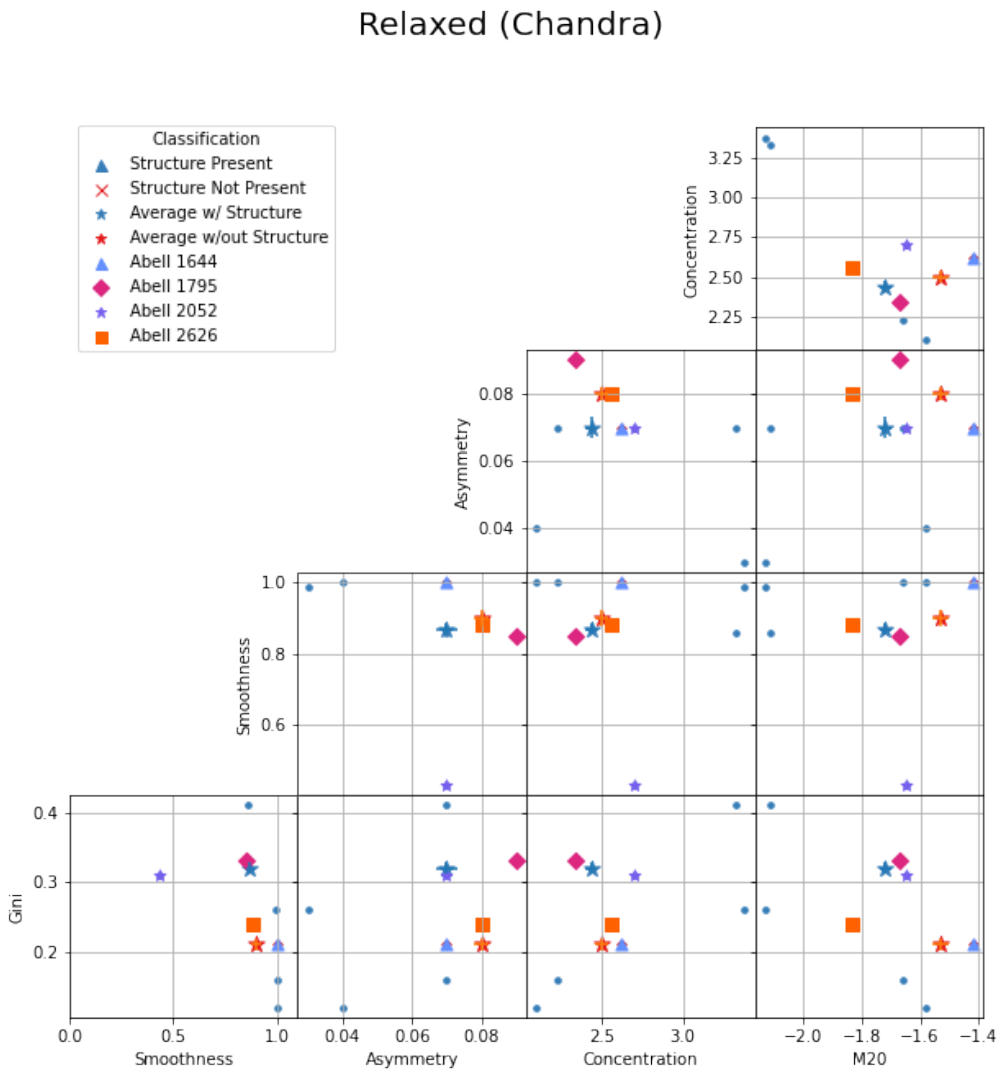

Figure C.6: Relaxed clusters show lower C and M_{20} and higher G values. Out of the well-known clusters, only Abell 1644 is disturbed and shows high M_{20} and low G. Out of the relaxed well-known clusters, none of them have high C and their G and M_{20} values are not definitive as some are high, whilst others are low. Because the relaxed/disturbed sample has to be confirmed by literature, this has removed a large portion of the disturbed clusters from the sample so these results for *Chandra* are not a good test for the trends in the parameters as there is not an even split.

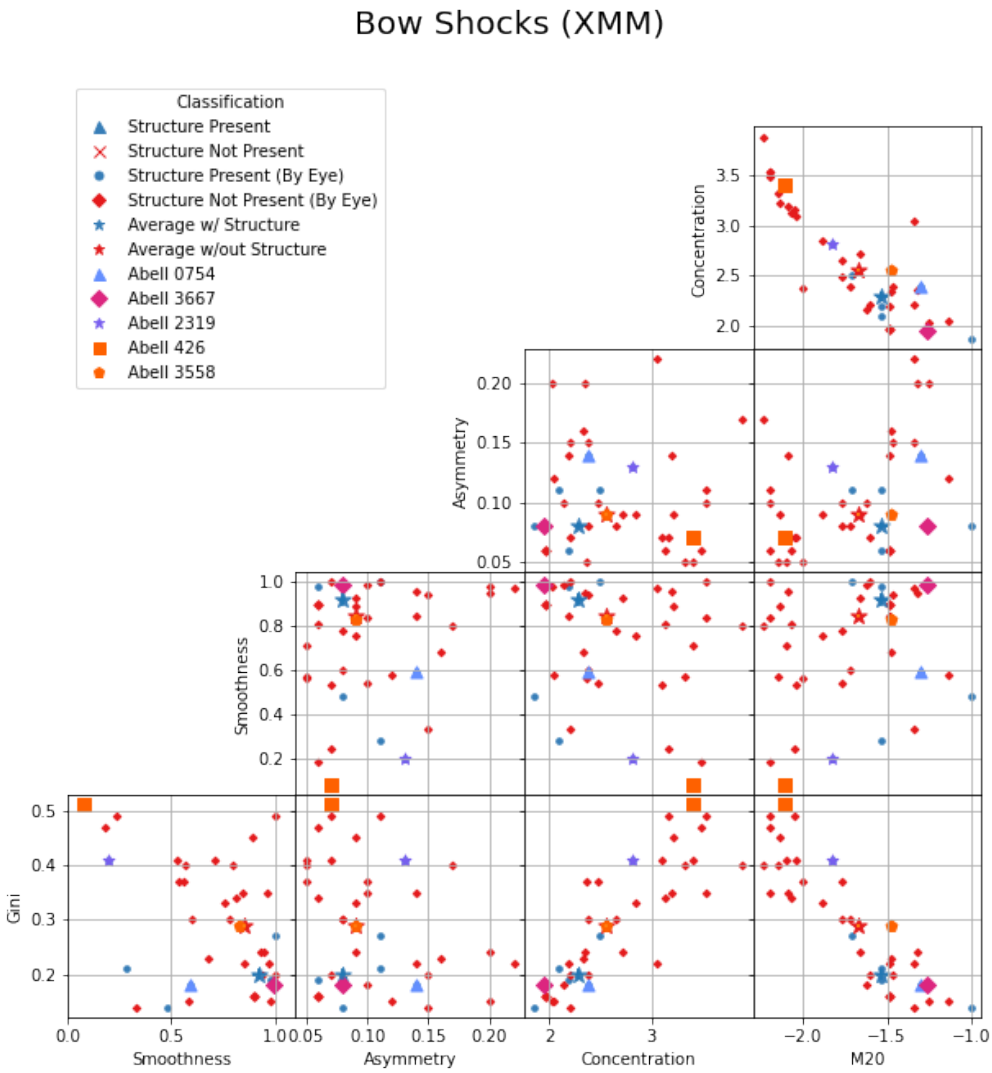

Figure C.7: Bow shocks have slight differences between the parameters M_{20}, G and C in which clusters with bow shocks have higher M_{20}, and lower G and C values. Well-known clusters with bow shocks confirmed by literature are Abell 754 and Abell 3667, these clusters follow this trend of parameters. Whereas, Abell 2319 which was determined to potentially have a bow shock by-eye, actually has the opposite trend which means it may not have a bow shock after all.

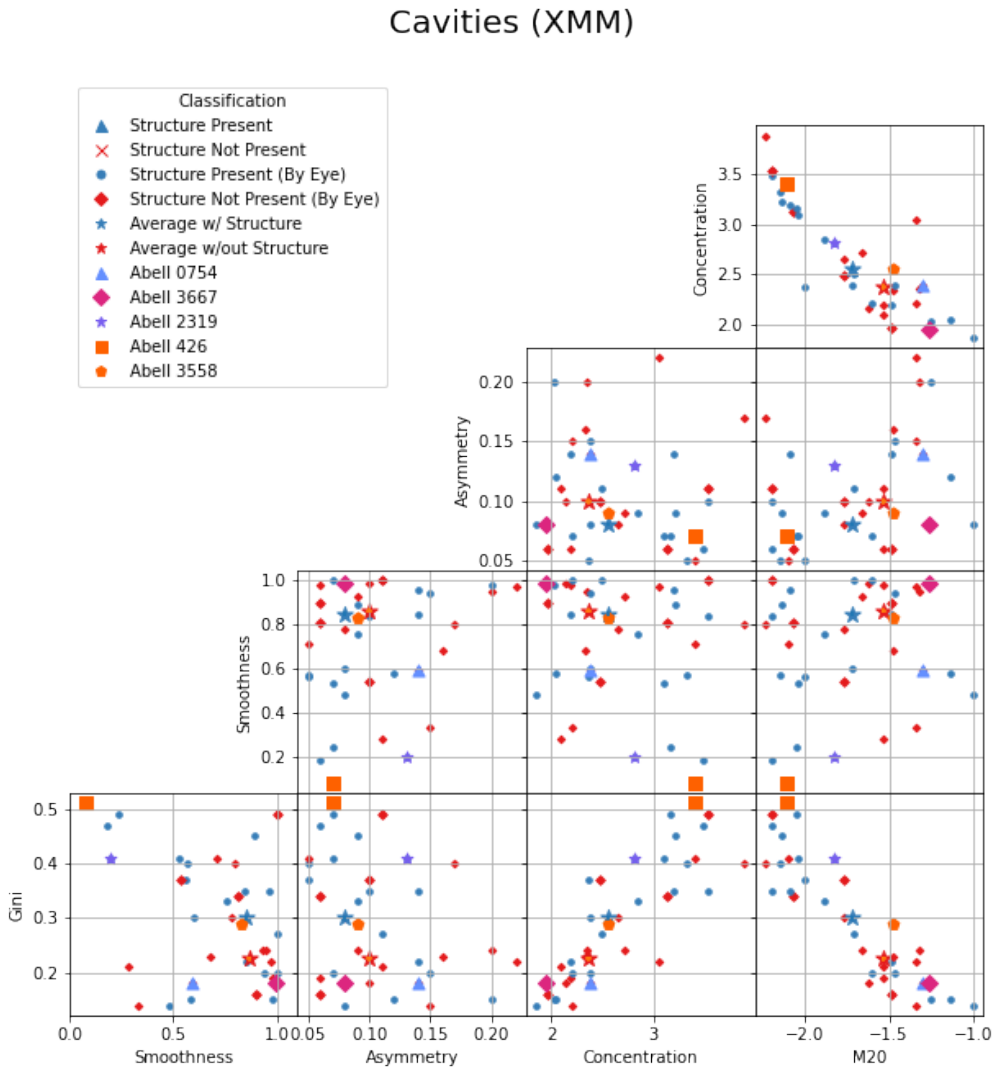

Figure C.8: Cavities show higher G and C values but lower M_{20} values. Abell 426 has cavities confirmed by literature and follows the trend perfectly.

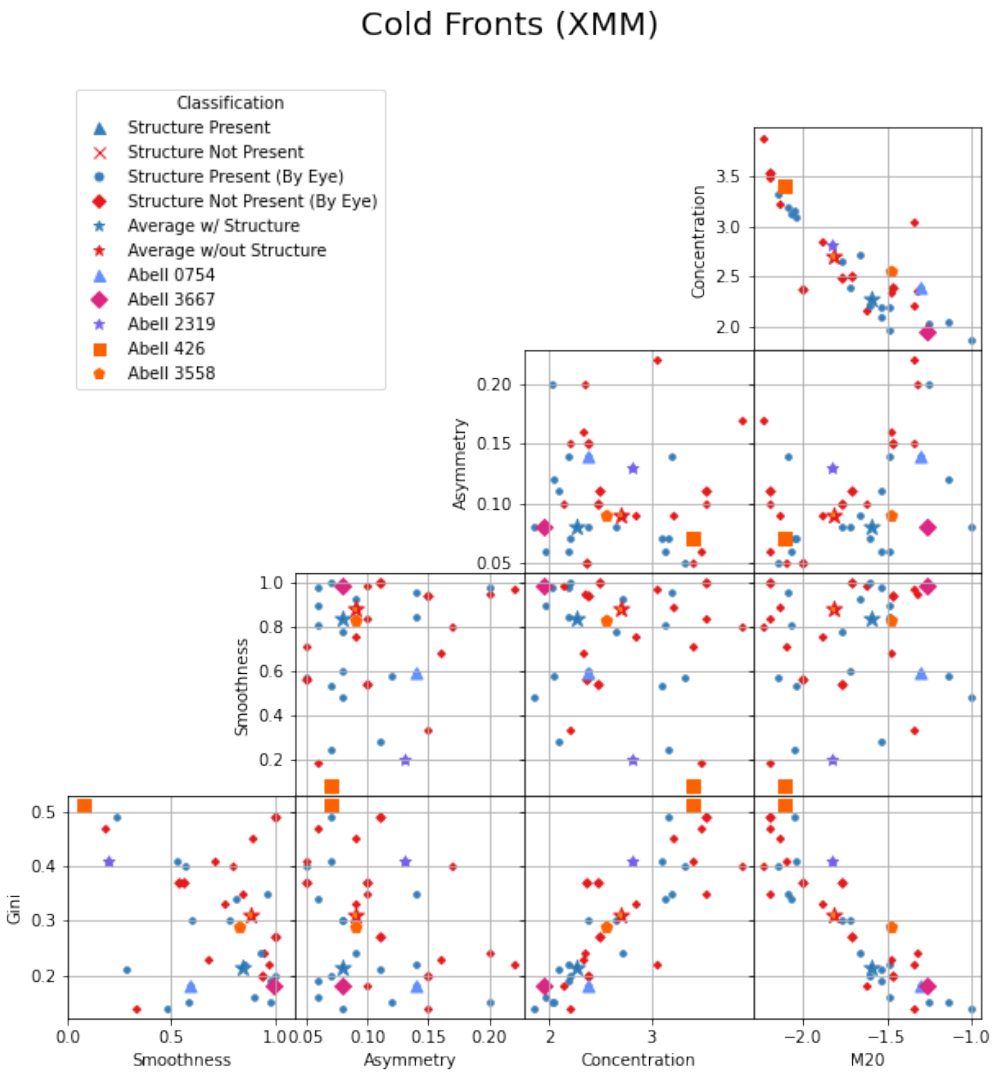

Figure C.9: Clusters with cold fronts show higher M_{20} values and lower G and C values. Abell 3667 may have a cold front and follows this trend which is promising. The other well-known clusters also follow this trend except for Abell 426 and 2319.

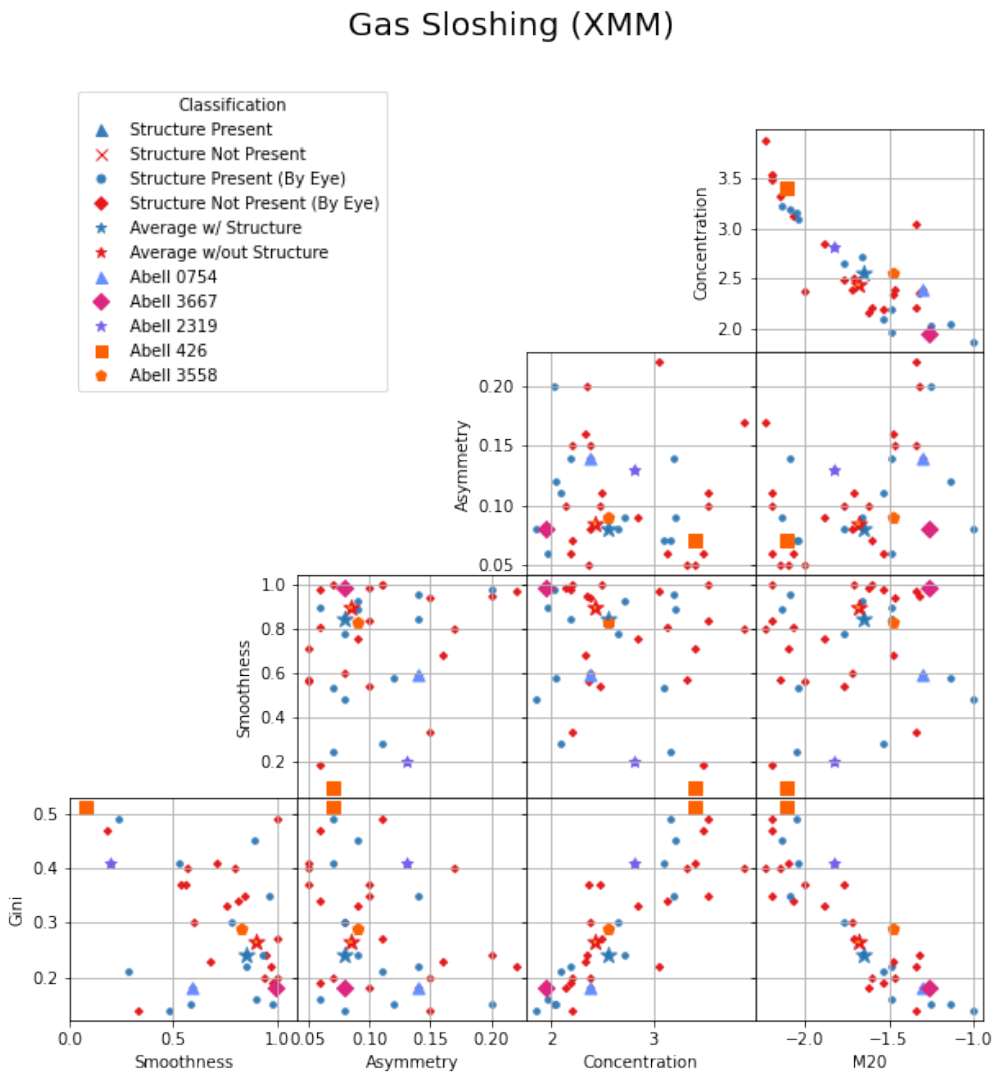

Figure C.10: Clusters that contain sloshing gas have very slightly lower G and M_{20} values. Again, we would argue that the samples are indistinguishable. This has not been improved by the separation of the telescopes which suggests resolution and depth are comparable.

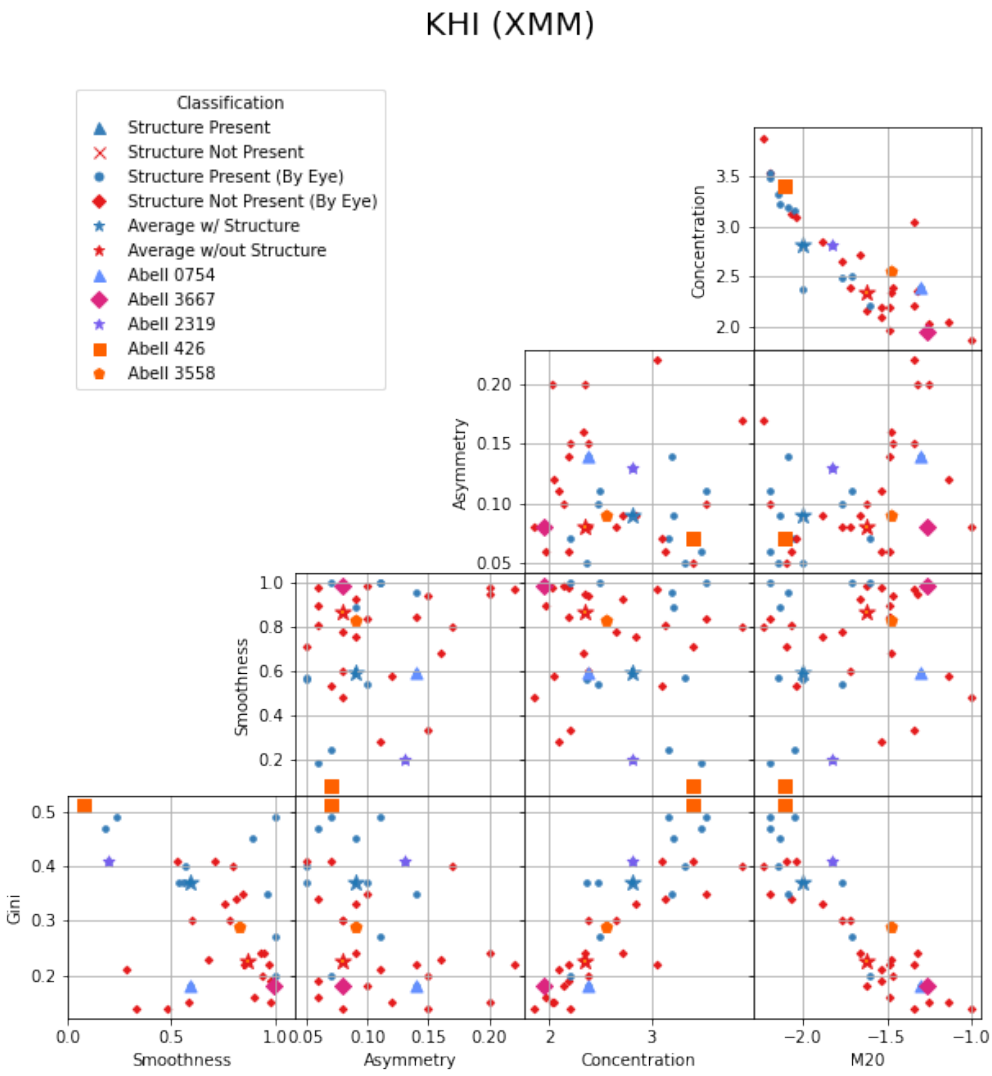

Figure C.11: Clusters that have KHI present have higher C and G values but lower M_{20} and S values. Abell 2319 and Abell 426 both have KHI confirmed by literature and both strongly follow this trend. This combined with K-S test results is promising.

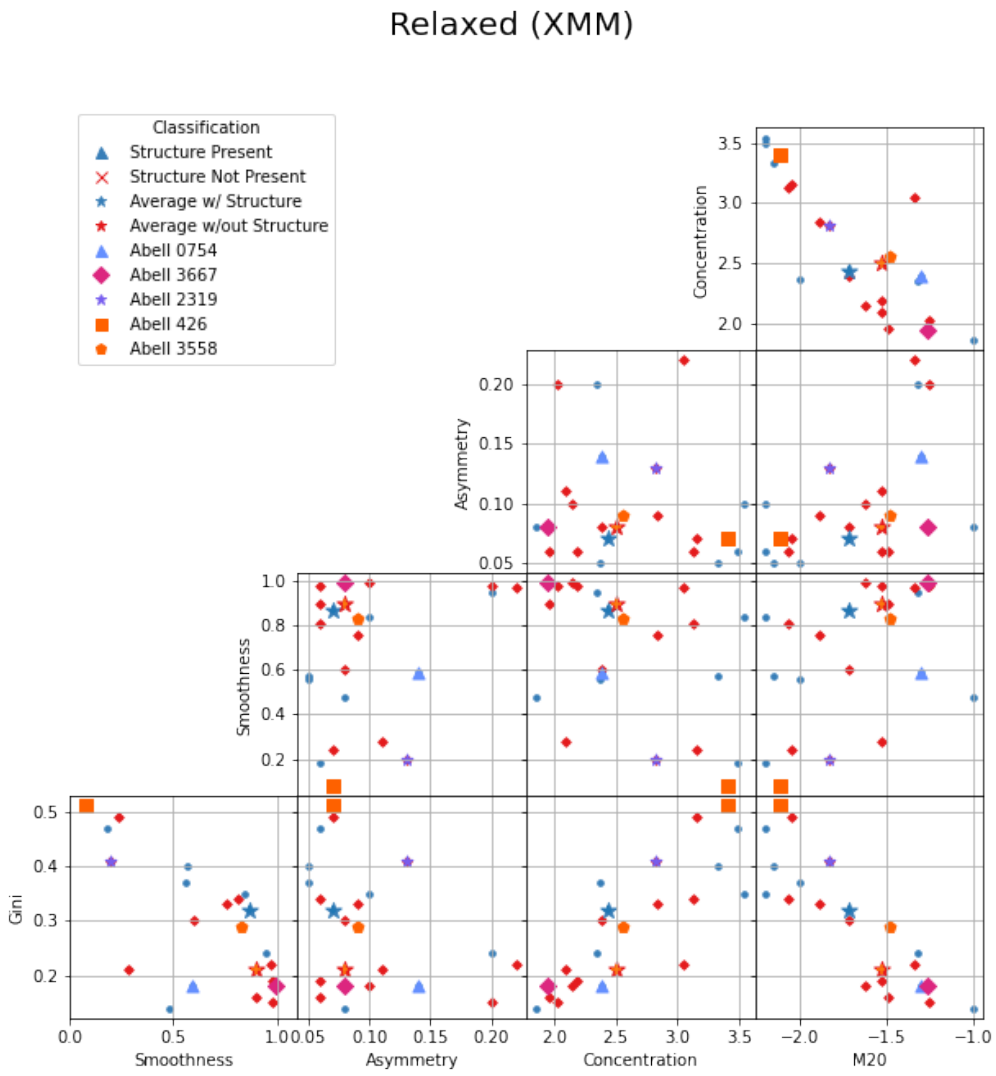

Figure C.12: Relaxed clusters show lower C and M_{20} and higher G values. The only relaxed well-known cluster in this sample is Abell 426 and this also follows the trend for relaxed clusters well. The disturbed clusters almost exactly oppose this trend.